

Closed-Loop Aeromaneuvering for a Mars Precision Landing¹

Roy Smith

CCEC-96-0205

Center for Control Engineering and Computation
University of California, Santa Barbara

¹This work supported by the Mars Exploration Technology Program at JPL

Abstract

The objective of this work is to investigate the use of feedback control in a Mars precision landing. The 1997 Pathfinder mission to Mars will use a bluff entry body on a ballistic trajectory. Errors in the atmospheric entry conditions (flight path angle, azimuth angle, and entry altitude) and uncertainties in the atmospheric properties and vehicle aerodynamics translate to a target accuracy of approximately 300 km by 50 km.

The work presented here is an initial investigation into the control of the aerodynamic entry phase. The ultimate objective is to reduce the landing errors to the order of tens or even one kilometer, and to outline the resulting technological requirements.

A preliminary study of the Pathfinder vehicle illustrates that in its present configuration, control will not significantly improve the landing precision. The closed-loop control of a biconic lifting body, with a lift/drag ratio of 1.0, has also been studied. The initial simulations indicate that both directional pointing and range control are possible. The control authority appears to be sufficient to overcome the landing errors that would otherwise arise from flight path angle errors at the atmospheric entry point. The open research issues in this problem are summarized and discussed.

Contents

1	Introduction	5
2	Outline of the Simulation Based Analysis	7
2.1	Dynamic Equations for Simulation	8
2.1.1	Input, output and state variable definitions	8
2.1.2	Equations of motion	10
2.2	Model of the Martian Environment	14
3	Vehicle Characteristics	16
3.1	Aerodynamic Coefficients and Mass Properties	17
3.1.1	Ballistic vehicles: Pathfinder	17
3.1.2	Lifting vehicles: Biconic configuration	19
3.2	Circular Symmetry Issues	24
3.2.1	Definition of α_e and θ_N	25
3.2.2	Bank angle and lift direction relationships	26
4	Ballistic Trajectory Analysis	27
4.1	Nominal entry characteristics	28
4.2	Analysis of flight path and azimuth errors	31
4.3	Control options for the ballistic vehicle	32
5	Controlled Lifting Vehicles	34
5.1	Directional Targeting Approaches	34

5.1.1	Control of ϕ_N	34
5.2	Attitude Control	36
5.2.1	Bank angle control	36
5.2.2	Lift vector control	37
5.3	Preliminary Simulation Results	40
5.3.1	Directional tracking study	40
5.3.2	Range authority study	44
6	Research Issues	47
6.1	A Summary of the Results	47
6.2	Immediate Research Issues	48
6.3	Longer Term Research Areas	50
	Acknowledgements	54
	References	54

1 Introduction

This work investigates the use of feedback control for a precision landing on Mars. The proposed mission will include a controlled atmospheric entry directly from interplanetary cruise (i.e. without first going into orbit). Atmospheric aeromaneuvering will be used to decelerate the vehicle and guide it to a prespecified terminal point above the surface. At that point a parachute will be deployed to further decelerate the vehicle. An engine will be used for the final descent, from approximately 5km to the surface. The ultimate objective is to perform a soft landing at a specified location, to an accuracy of the order of tens or even one kilometer.

The work described here investigates only the aeromaneuvering control aspect of this problem. The vehicle entry into the upper atmosphere of Mars is the starting point for the simulations presented here. At the entry point there will be errors between the planned and actual entry conditions. The prior navigation calculations can be used to estimate these errors—it is the function of the aerodynamic control phase to compensate for the known and unknown errors. This compensation must take place in an uncertain atmosphere, with vehicle dynamics that are also somewhat uncertain. Closed-loop control of the entry phase is essential for dealing with the entry errors and system uncertainty.

The 1997 Pathfinder mission to Mars will use a bluff entry body on a ballistic trajectory. The errors in the atmospheric entry conditions (flight path angle, azimuth angle, and entry altitude) and uncertainties in the atmospheric properties and vehicle aerodynamics translate to a target accuracy of approximately 300 km by 50 km.

Two scenarios are studied via simulation. The first involves the Pathfinder vehicle in its present configuration. It illustrates that the control authority is such that no significant improvement in landing precision is possible. Note that this is a vehicle designed for a ballistic entry. The nominal angle-of-attack is zero degrees and in this configuration the lift/drag ratio is almost zero. Future work may consider this vehicle with a center of mass offset which will increase its angle-of-attack and lift/drag ratio. Whether or not such modifications are sufficient to control purposes remains to be seen.

The second vehicle is based on an earlier Mars Sample Return Mission design. The vehicle is a large biconic with a lift/drag ratio of approximately 1.0. The control authority is significant and the initial simulations indicate that closed-loop control of this vehicle is capable of overcoming the landing errors that would otherwise result from entry point errors. Both directional pointing and range control can be achieved via a modulated bank angle strategy.

Similar approaches have been considered in a number of other applications. Lifting trajectories have been used in the Apollo, Shuttle and Viking programs. See Dierlam [1], and the references therein, for more detail on the strategies used in these cases. Although the Viking program placed vehicles on Mars, these were not precision landings [2]. An open-loop strategy was used and the $3\text{-}\sigma$ ellipse was of the order of $120\text{ km} \times 60\text{ km}$. The Apollo program used a low L/D ratio (0.3) vehicle and bank angle control to maintain a reference drag profile. Crossrange requirements were met by changing the sign of the bank angle in response to current crossrange error. The desired landing accuracy was 15 nautical miles.

The Shuttle program uses a vehicle with an approximate L/D ratio of 1.2 and has significantly greater accuracy requirements. Control is implemented via bank angle, angle-of-attack and a speed brake, which are used to fly reference drag and altitude rate profiles. In the case of Earth re-entry a better characterization of the atmosphere is available, reducing the uncertainty associated with the problem.

Dierlam [1] describes a simulation study of a bank angle control strategy for landing a vehicle on Mars. A predictor-corrector strategy is used to predict the terminal errors which result from the currently estimated trajectory errors and forms the basis of the control algorithm. This work uses a three degree of freedom simulation and does not consider the effects of uncertainty on vehicle orientation. The use of a predictor-corrector based guidance algorithm for aerobraking in the Martian atmosphere has been considered by Braun and Powell [3]. They also present a six degree of freedom analysis of a guidance algorithm for Mars aerocapture [4]. The vehicle under consideration is much larger than those considered here, and the mission objective is significantly different.

The work presented here develops a six degree of freedom simulation and also investigates nonlinear attitude control strategies. This work is preliminary and serves mostly to illustrate the potential areas of future work. The open research issues in this problem are summarized and discussed.

Section 2 discusses the simulation models in detail. The inputs, outputs and state variables are defined and the equations of motion are presented. The assumptions used in the derivation of these equations are explicitly listed as several small effects are neglected for simplicity. The model of the Martian atmosphere is also given. Section 3 describes the Pathfinder and biconic vehicles in detail and presents the aerodynamic and mass properties of each vehicle. Both vehicles are circularly symmetric and the issues which arise from this are also discussed.

The simulation analysis of the ballistic trajectory, using the Pathfinder vehicle, is pre-

sented in Section 4. The lifting biconic vehicle trajectory is studied in Section 5. This section also provides details on the control algorithms used for both attitude and directional tracking. Section 6 provides a summary of the results and gives a detailed outline of the future research issues.

2 Outline of the Simulation Based Analysis

The following effects are considered in these equations:

- An exponential atmospheric density;
- The curvature of Mars;
- The angular rotation of Mars (Coriolis effects);
- Aerodynamic forces (lift, drag, side force) as a function of angle of attack and sideslip angle;
- Aerodynamic moments (roll, pitch and yaw moments) as a function of angle of attack and sideslip angle;
- Mass changes in the spacecraft due to thruster firings.

The following aspects are not considered in the equations:

- Centripetal force ($\omega \times (\omega \times r)$);
- The dependence of the aerodynamic coefficients on velocity or Mach number;
- The rotation of Mars around the sun;
- Wind in the atmosphere;
- Non-spherical planet;
- Flexibility or articulated components in the vehicle.

The simulations use modular function calls to evaluate the planet characteristics (atmospheric density, altitude, gravitational force) and vehicle properties (aerodynamic coefficients, mass, moments of inertia). This makes it relatively straightforward to incorporate more detailed planet models (MARSGRAM for example) and different vehicles in the simulation.

2.1 Dynamic Equations for Simulation

The primary references for the material presented here are Etkin [5] and Boussalis [6]. The definitions of the various frames of reference are presented in more detail in the above.

2.1.1 Input, output and state variable definitions

To begin define the system variables that will form a “state” vector for the dynamic system. The velocity vector has three components in the body axis system,

- u component in x_B direction [km/sec]
- v component in y_B direction [km/sec]
- w component in z_B direction [km/sec]

The angular velocities about the body axes are defined as

- p roll rate (around x_B axis) [rad/sec]
- q pitch rate (around y_B axis) [rad/sec]
- r yaw rate (around z_B axis) [rad/sec]

The Euler angles are the rotation of the body frame with respect to the local vertical frame.

- ϕ bank angle (rotation about x_V) [rad]
- θ elevation angle (rotation about y_V) [rad]
- ψ azimuth angle (rotation about z_V) [rad]

The vehicle center of mass position is specified in planetary coordinates.

- R radial distance from center of Mars [km]
- λ latitude [rad]
- μ longitude [rad]

The final state variable is the vehicle mass which will vary if thrusters are used for control.

m vehicle mass [kg]

For the vehicle 2 configuration (lifting body), thrusters were used for control actuation. In this case there are six control inputs.

T_x thrust in x_B axis direction [N]
 T_y thrust in y_B axis direction [N]
 T_z thrust in z_B axis direction [N]
 M_x roll moment input (about x_B axis) [Nm]
 M_y pitch moment input (about y_B axis) [Nm]
 M_z yaw moment input (about z_B axis) [Nm]

All six inputs are given in the equations for generality. None of the vehicles considered here make use of all six.

The simulation outputs, listed in the component order of the output vector, are:

R_v altitude above mean planet surface [km]
 λ latitude [deg]
 μ longitude [deg]
 V velocity magnitude [km/sec]
 ψ_W heading angle [deg]
 γ_W flight path angle [deg]
 σ_W bank angle [deg]
 α angle of attack [deg]
 β side slip angle [deg]
 p roll rate [deg/sec]
 q pitch rate [deg/sec]
 r yaw rate [deg/sec]
 m mass [kg]
 F_L lift force [N]
 F_D drag force [N]
 F_Y side force [N]
 L total roll moment [Nm]
 M total pitch moment [Nm]
 N total yaw moment [Nm]

Note that for convenience the altitude, R_v , is with respect to the surface, so $R_v = R - R_p$, where R_p is the mean planet radius, given in Section 2.2. The environmental parameters

are also generated as simulation outputs.

ρ density [kg/km³]
 Q dynamic pressure [kg/km/sec²]
 g local gravitational constant [km/sec²]

2.1.2 Equations of motion

To define the simulation dynamics we must calculate the state variable derivatives as a function of the current state variable values and the inputs, and the outputs as a function of the state and input variables.

Several intermediate calculations are required. Define V as the magnitude of the velocity vector,

$$V = (u^2 + v^2 + w^2)^{1/2}.$$

We can now calculate the aerodynamic angles,

$$\begin{aligned}\alpha &= \arctan(w/u) \\ \beta &= \arcsin(v/V)\end{aligned}$$

The dynamic pressure is given by

$$Q = \frac{\rho V^2}{2},$$

where ρ is the atmospheric density (which is a function of vehicle altitude).

We can now calculate the aerodynamic forces on the center of mass.

$$\begin{aligned}F_L &= QSC_L \\ F_D &= QSC_D \\ F_Y &= QSC_Y\end{aligned}$$

The reference area, S , for each vehicle is given in Section 3.1. The force coefficients, C_L , C_D and C_Y , are a function of the effective angle of attack and are also discussed in Section 3.1.

We can similarly calculate the aerodynamic moments acting on the vehicle.

$$\begin{aligned} M_L &= QbSC_l \\ M_M &= QcSC_m \\ M_N &= QbSC_n \end{aligned}$$

Again, the reference lengths and coefficients for each vehicle are discussed in Section 3.1.

To simplify the following, we give the coordinate transformations between the various reference frames that are used here. The transformations are constructed from simple rotations. The rotation about the first component axis is given by,

$$L_1(\theta) = \begin{bmatrix} 1 & 0 & 0 \\ 0 & \cos \theta & \sin \theta \\ 0 & -\sin \theta & \cos \theta \end{bmatrix}.$$

The second and third component axis rotations are

$$L_2(\theta) = \begin{bmatrix} \cos \theta & 0 & -\sin \theta \\ 0 & 1 & 0 \\ \sin \theta & 0 & \cos \theta \end{bmatrix},$$

and

$$L_3(\theta) = \begin{bmatrix} \cos \theta & \sin \theta & 0 \\ -\sin \theta & \cos \theta & 0 \\ 0 & 0 & 1 \end{bmatrix}.$$

The transformation from wind to body axes is given by

$$L_{BW} = L_2(\alpha)L_3(-\beta).$$

The order of the elementary rotations is critical. The inverse transformation, L_{WB} , is simply the transpose of the above,

$$L_{WB} = L_{BW}^{-1} = L_{BW}^T.$$

The transformation from the local vertical to body axis frames is

$$L_{BV} = L_1(\phi)L_2(\theta)L_3(\psi),$$

and the transformation from a planet centered frame to the local vertical frame is given by

$$L_{VP} = L_2(\pi/2 - \lambda)L_3(-\mu)L_1(\pi)L_3(\pi/2).$$

We are now in a position to calculate the state vector derivatives.

$$\begin{aligned} \begin{bmatrix} \dot{u} \\ \dot{v} \\ \dot{w} \end{bmatrix} &= \frac{1}{m} \left(L_{BW} \begin{bmatrix} -F_D \\ -F_Y \\ -F_L \end{bmatrix} + \begin{bmatrix} T_x \\ T_y \\ T_z \end{bmatrix} + m L_{BV} \begin{bmatrix} 0 \\ 0 \\ g \end{bmatrix} \right) \\ &\quad - \left(\begin{bmatrix} p \\ q \\ r \end{bmatrix} + L_{BV} L_{VP} \begin{bmatrix} 0 \\ 0 \\ \omega_P \end{bmatrix} \right) \times \begin{bmatrix} u \\ v \\ w \end{bmatrix}. \end{aligned}$$

In the above \times denotes the vector cross product and ω_p is the rotation rate of the planet (given in Section 2.2).

The body axis moments are made up of the aerodynamic moments and the applied control moments.

$$\begin{bmatrix} L \\ M \\ N \end{bmatrix} = \begin{bmatrix} M_L \\ M_M \\ M_N \end{bmatrix} + \begin{bmatrix} M_x \\ M_y \\ M_z \end{bmatrix}.$$

The body axis rotation rate derivatives are given by

$$\begin{bmatrix} \dot{p} \\ \dot{q} \\ \dot{r} \end{bmatrix} = I^{-1} \left(\begin{bmatrix} L \\ M \\ N \end{bmatrix} - \begin{bmatrix} p \\ q \\ r \end{bmatrix} \times I \begin{bmatrix} p \\ q \\ r \end{bmatrix} \right).$$

The individual components of the inertia matrix,

$$I = \begin{bmatrix} I_x & -I_{xy} & -I_{zx} \\ -I_{xy} & I_y & -I_{yz} \\ -I_{zx} & -I_{yz} & I_z \end{bmatrix},$$

are given for each vehicle in Section 3.1.

The vehicle position, with respect to the planet, is calculated via,

$$\begin{bmatrix} \dot{R} \\ \dot{\lambda} \\ \dot{\mu} \end{bmatrix} = \begin{bmatrix} 0 & 0 & -1 \\ 1/R & 0 & 0 \\ 0 & 1/R \cos \lambda & 0 \end{bmatrix} L_{VB} \begin{bmatrix} u \\ v \\ w \end{bmatrix}.$$

The latitude and longitude derivatives are need to calculate the effect of the rotation of the planet in the body axes frame. From this, and the vehicle rotation rates, we can calculate the derivatives of the orientation angles. The relative body rotation rates are given by

$$\omega_{rel} := \begin{bmatrix} p \\ q \\ r \end{bmatrix} - L_{BV} \begin{bmatrix} (\omega_p + \dot{\mu}) \cos \lambda \\ -\dot{\lambda} \\ -(\omega_p + \dot{\mu}) \sin \lambda \end{bmatrix}.$$

Now,

$$\begin{bmatrix} \dot{\phi} \\ \dot{\theta} \\ \dot{\psi} \end{bmatrix} = \begin{bmatrix} 1 & 0 & -\sin \theta \\ 0 & \cos \phi & \sin \phi \cos \theta \\ 0 & -\sin \phi & \cos \phi \cos \theta \end{bmatrix}^{-1} \omega_{rel}.$$

The final state derivative is the mass. The total thrust, T , is given by

$$T = |T_x| + |T_y| + |T_z| \\ + |M_x|/A_x + |M_y|/A_y + |M_z|/A_z,$$

where A_x , A_y , and A_z are the length of the moment arms in the x , y and z directions. Now,

$$\dot{m} = -T/I_{sp},$$

where I_{sp} is the specific thrust for the engines, assuming that all are identical. The moment arms and specific thrust values used for the controlled vehicle are given in Section 3.1.

The output variables correspond closely to the state variables and usually involve only a change of units. The only exception to this is the calculation of the orientation angles in the wind frame. These are obtained from the L_{WV} transformation matrix in the following manner. The notation $L_{WV}(i, j)$ denotes the row i , column j element of the L_{WV} matrix. Observe that

$$\begin{aligned} L_{WV}(1, 3) &= -\sin \gamma_W \\ L_{WV}(1, 1) &= \cos \gamma_W \cos \psi_W \\ L_{WV}(1, 2) &= \cos \gamma_W \sin \psi_W \\ L_{WV}(2, 3) &= \sin \sigma_W \cos \gamma_W \\ L_{WV}(3, 3) &= \cos \sigma_W \cos \gamma_W, \end{aligned}$$

and so the orientation angles can be reconstructed via

$$\begin{aligned} \gamma_W &= \arcsin(-L_{WV}(1, 3)) \\ \psi_W &= \arctan\left(\frac{L_{WV}(1, 2)}{L_{WV}(1, 1)}\right) \\ \sigma_W &= \arctan\left(\frac{L_{WV}(2, 3)}{L_{WV}(3, 3)}\right) \end{aligned}$$

A four quadrant arctangent operation is required to prevent angle ambiguities.

2.2 Model of the Martian Environment

A simple exponential model was used for the density of the Martian atmosphere. This is an exponential model with a reference radius, R_r , and density, ρ_r ,

$$\rho = \rho_r e^{-0.1(R-R_r)},$$

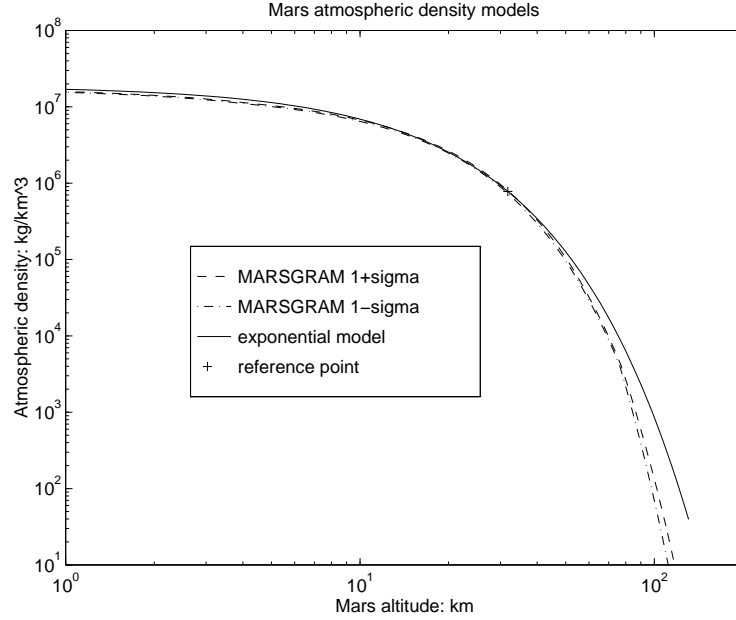


Figure 1: Martian atmospheric density, exponential and MARSGRAM models (note logarithmic scales)

where R is the vehicle altitude, expressed as a radius from the planet center. The reference altitude and density were,

$$\begin{aligned} R_r &= 3,4290.0 \text{ km} \\ \rho_r &= 7.8 \times 10^5 \text{ kg/km}^3. \end{aligned}$$

The mean planetary radius, R_p , is 3,397.2 km which makes the reference altitude 31.8 km above the planet surface.

Figure 1 illustrates the density altitude relationship on a logarithmic scale. The exponential density model is reasonably close to the MARSGRAM $1+\sigma$ and $1-\sigma$ density profiles.

The gravitation model used is a simple inverse square law.

$$g = \frac{\mu}{R^2},$$

where

$$\mu = 4.28283 \times 10^4 \text{ km}^3/\text{s}^2.$$

It is standard to denote the gravitational constant by μ , which should not be confused with same notation for longitude used in the equations of motion.

The length of the Martian day is 24.62294 hours which gives a rotation rate of

$$\omega_p = 7.0882 \times 10^{-5} \text{ radians/second.}$$

3 Vehicle Characteristics

We are primarily interested in vehicles that are capable of generating significant lift forces. A bluff entry body on a ballistic trajectory was also studied initially as a means of checking the simulation against a known mission profile. The 1997 Pathfinder entry body was used for this purpose.

The vehicle used for the majority of this study was a biconic vehicle, initially proposed for a Mars Sample Return Mission. The aerodynamic properties of this form of vehicle were studied extensively by Boussalis [6, 7, 8], and this work provides a basis for the current study. Ultimately we will consider different vehicle configurations, including the addition of aerodynamic control surfaces.

Both vehicles are circularly symmetric. The simulation program does not rely on this being the case and non-symmetric or winged vehicles can easily be considered. The particular control algorithms studied do take advantage of the circularly symmetric configuration. The principles behind these algorithms can be adapted to other configurations.

Neither vehicle is well suited for a potential precision landing mission; the Pathfinder has insufficient control authority and the biconic vehicle is too large and probably too light for this type of mission. This study is an initial investigation into the aeromaneuvering control capabilities and these vehicles were chosen for investigation because aerodynamic models were readily available. The design of an appropriate vehicle configuration is an important future research topic.

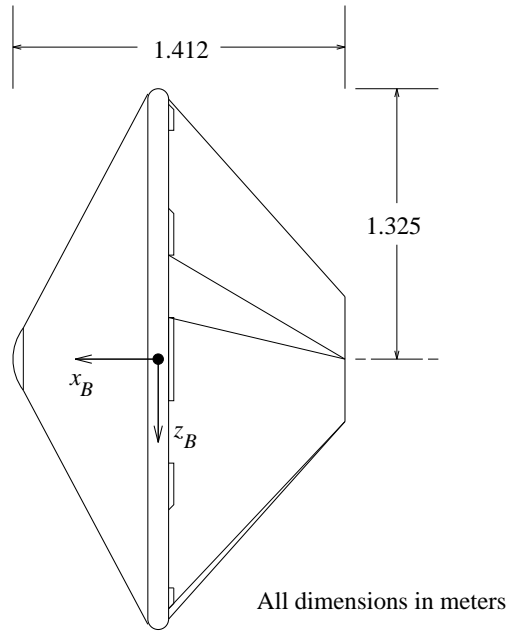


Figure 2: Pathfinder entry vehicle configuration

3.1 Aerodynamic Coefficients and Mass Properties

The most significant feature of the symmetric configuration is the fact that sideslip angle (β) and angle-of-attack (α) have identical effects. The results from the fact that the definition of the vehicle vertical direction is arbitrary. The consequences of this are discussed further in Section 3.2.

3.1.1 Ballistic vehicles: Pathfinder

The Pathfinder entry vehicle, illustrated in Figure 2, was considered as detailed aerodynamic and configuration information is available in the work of Braun *et al.* [9], and Spencer and Braun [10].

The vehicle mass and inertia properties used in the simulations are given below. The Pathfinder design has evolved through several configurations, masses and axes definitions. Our choices of axes matches that given in Section 2.1, and the values are those given in [9].

Mass (kg)	552.0					
Inertias (kg.m ²)	I_x	I_y	I_z	I_{yz}	I_{xy}	I_{zx}
	230.0	184.0	180.0	0.0	0.0	0.0

The aerodynamic coefficients are available as a function of α and Mach number. We have approximated these coefficients by the following relationships.

$$\begin{aligned}
\text{Drag:} \quad C_D &= 1.6, \\
\text{Lift:} \quad C_L &= -0.025\alpha, \\
\text{Roll moment:} \quad C_l &= 0.0, \\
\text{Pitch moment:} \quad C_m &= -0.02\alpha.
\end{aligned}$$

Because of circular symmetry, the side force and yaw moment coefficients, C_Y and C_n , are equal to the lift and pitch moment coefficients, C_L and C_m , respectively, with α being replaced by $-\beta$. For simplicity in the following discussion, we will assume that the bank angle, ϕ , is zero. In other words the vehicle z_B axis points directly downward.

To complete the force calculations the aerodynamic reference areas are needed. These are given below.

Reference area (m ²)	S	5.515
Roll/yaw reference length (m)	b	2.65
Pitch reference length (m)	c	2.65

The lift/side force coefficients are illustrated graphically in Figure 3. This illustrates the relative size and vector direction of the C_L , C_Y combination. This figure can be interpreted by considering the velocity vector as pointing directly at the viewer from the origin. If the vehicle x_B (“forwards”) axis is not aligned with the velocity vector (i.e α and/or β non zero), then the coordinates $(\sin \beta, \sin \alpha \cos \beta)$ gives the normalized position of the vehicle nose. The stem of each arrow is placed on the vehicle nose and the arrow then gives the relative size and direction of the force acting on the vehicle center of mass.

The symmetry is obvious in the figure. Note also that the vehicle has a negative lift coefficient. For example, if the nose is down ($\alpha < 0$, $\beta = 0$), the resulting force is upwards. This results from the fact that the axial aerodynamic force is far greater than the normal aerodynamic force, and is a common feature of bluff aerodynamic bodies. Slender or winged vehicles typically have positive lift coefficients.

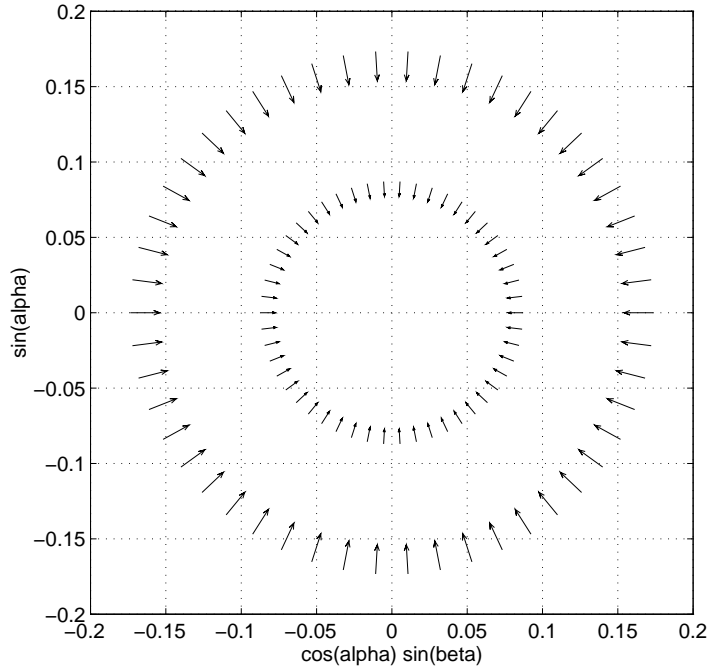


Figure 3: Pathfinder vehicle: lift/side force vector as a function of nose position

The pitch/yaw characteristics can be illustrated graphically in the same manner. This is done in Figure 4. Again, we can picture this as a front-on view with the velocity vector at the origin. In this case we are considering moments on the vehicle and the arrows illustrate the direction that the vehicle nose would move and the relative size of the moment.

This vehicle has a static trim angle of $\alpha = 0$ degrees. For example, if the nose is up ($\alpha > 0, \beta = 0$) the moment acts in the direction of pushing the nose down. Clearly, the origin ($\alpha = 0, \beta = 0$) is a stable static equilibrium point.

3.1.2 Lifting vehicles: Biconic configuration

The details provided here have developed in earlier work by Boussalis [6, 7, 8]. The vehicle is illustrated in Figure 5.

The inertia was approximated by using the standard formulae for a cylinder of length l ,

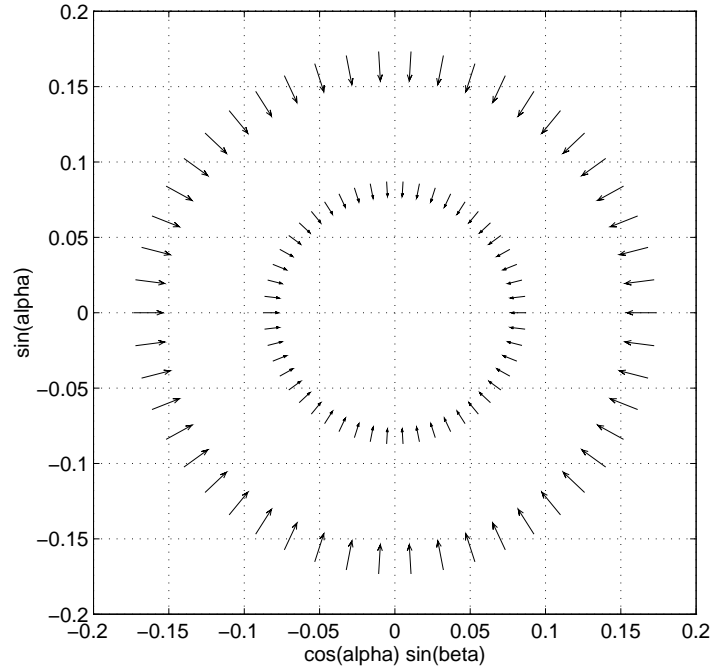
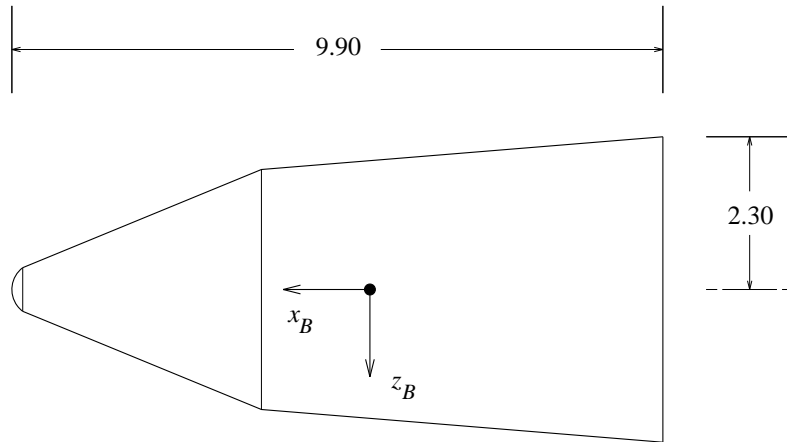


Figure 4: Pathfinder vehicle: pitch/yaw moment vector as a function of nose position



All dimensions in meters

Figure 5: Biconic entry vehicle configuration

radius r , and mass m .

$$I_x = \frac{mr^2}{2},$$

$$I_y = \frac{m}{12}(3r^2 + l^2),$$

$$I_z = \frac{m}{12}(3r^2 + l^2).$$

The radius was selected as the average of the bases of the two cones ($r = 2.085$ meters) and l was chosen as the length of the vehicle ($l = 9.9$ meters). This gives the following values.

Mass, m (kg)	500.0					
Inertias (kg.m ²)	I_x	I_y	I_z	I_{yz}	I_{xy}	I_{zx}
	1086.8	4627.2	4627.2	0.0	0.0	0.0

The following aerodynamic reference area and lengths were chosen for this vehicle.

Reference area (m ²)	S	16.619
Roll/yaw reference length (m)	b	32.8915
Pitch reference length (m)	c	32.8915

The lateral aerodynamic coefficients were previously calculated from hypersonic Newtonian impact theory and are given in [7]. Also given was a polynomial approximation (third or fourth order depending upon the coefficient in question) as a function of α . Rather than giving the full polynomial, we present the data graphically.

Figure 6 provides a vector illustration of the lift and side force coefficients (C_L and C_Y) as a function of the position of the vehicle nose. The interpretation is the same as Figure 3 for the Pathfinder vehicle.

Again the symmetry in the figure is evident. In the biconic case the coefficient of lift is positive, which is more in keeping with our intuition of flying vehicles.

The pitch and yaw coefficients are similarly illustrated in Figure 7. This figure is analogous to Figure 4 for the Pathfinder case.

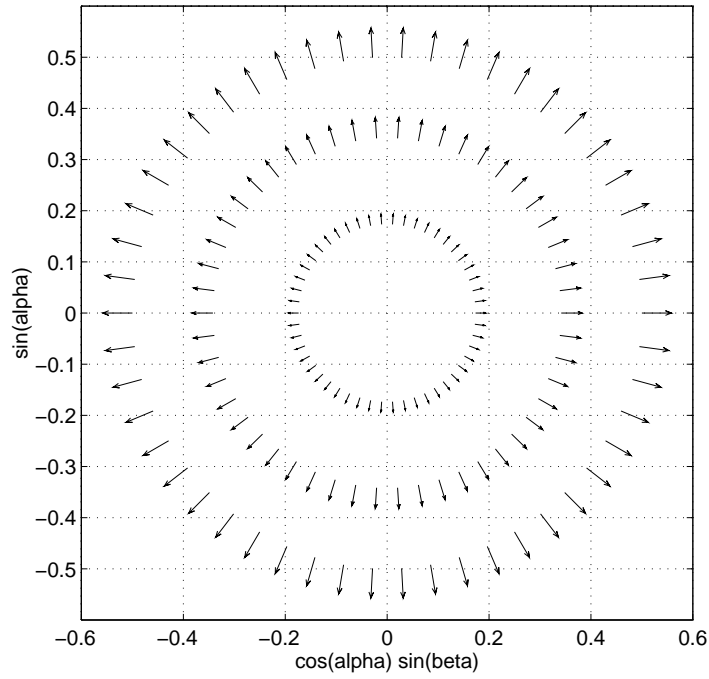


Figure 6: Biconic vehicle: yaw/side force vector as a function of nose position

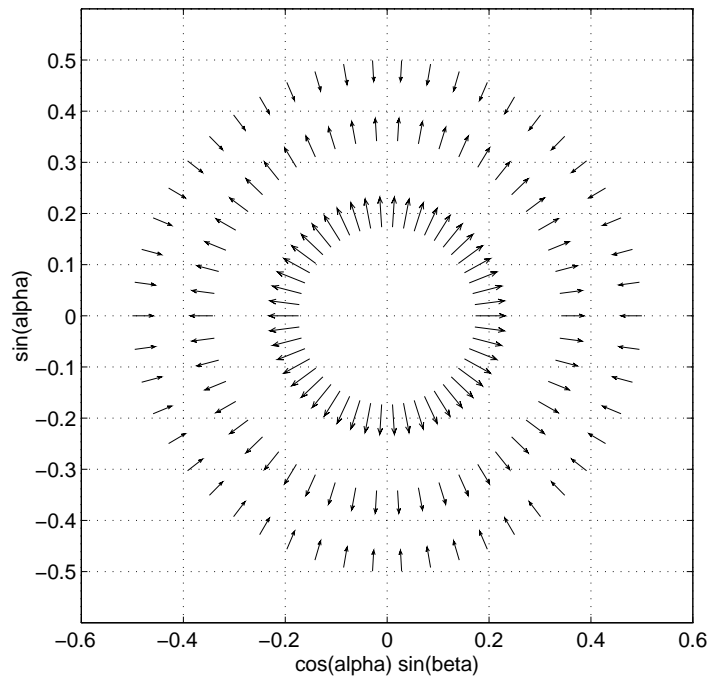


Figure 7: Biconic vehicle: pitch/yaw moment vector as a function of nose position

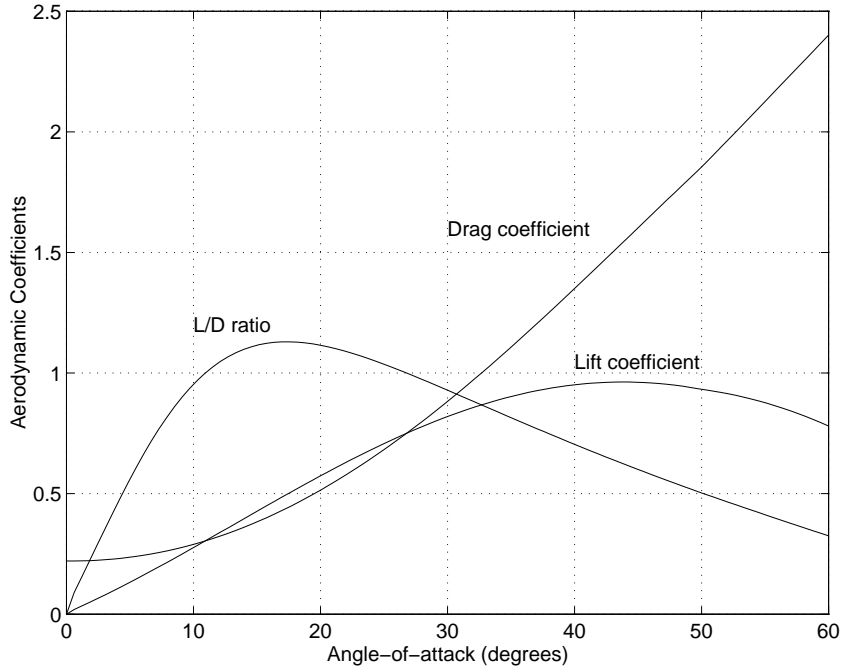


Figure 8: Biconic vehicle: aerodynamic force coefficients: C_L , C_D , and L/D ratio

There are significant differences in the pitch/yaw properties in the biconic case. Although it is not immediately obvious in Figure 7, the origin ($\alpha = 0$, $\beta = 0$) is now an unstable equilibrium. There is a stable equilibrium and it corresponds to a circle of radius 26 degrees (approx.). This is the trim angle-of-attack, and as the figure shows, from a stability point of view there is no distinction between the point $\alpha = 26$, $\beta = 0$ and the point $\alpha = 0$, $\beta = 26$ (or any other points on the circle). The existence of this family of equilibria is important for the development of the control algorithms. Section 3.2 will expand on these issues.

For lifting vehicles we are also interested in the values and relative sizes of lift and drag coefficients (C_L and C_D) as a function of α . These are illustrated in Figure 8.

The biconic vehicle has a maximum lift/drag ratio of about 1.1 at approximately 18 degrees angle-of-attack. Although this is significantly larger than the Pathfinder, it is still small compared to typical atmospheric flying vehicles, which might have L/D ratios in the range 3 to 5. For a comparison between aerodynamic re-entry vehicles, the Apollo re-entry vehicle has an L/D ratio of 0.3 and the Shuttle orbiter has an L/D ratio of 1.2 [1].

Figure 8 also illustrates that for zero angle-of-attack there is no lift (C_L is zero). However

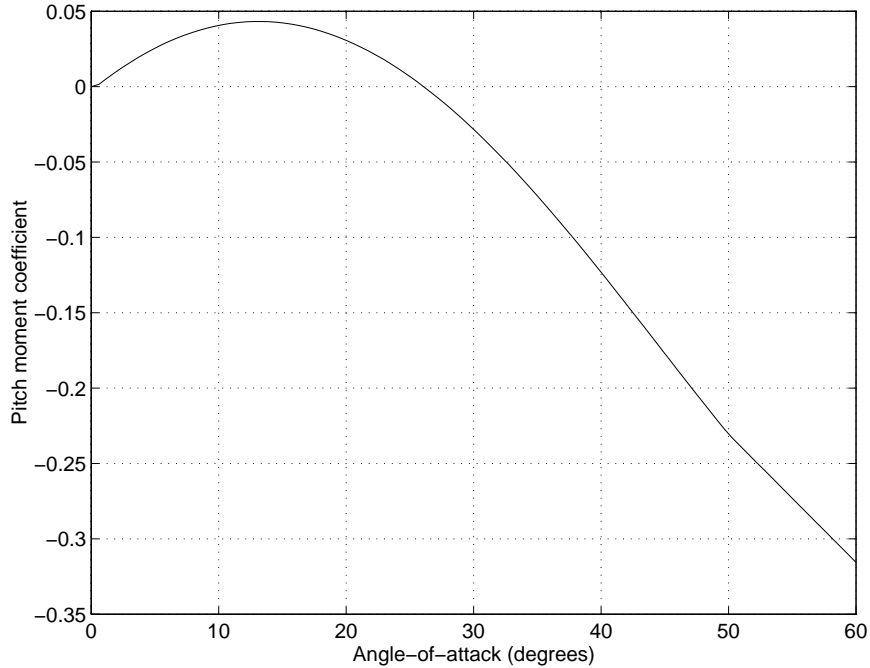


Figure 9: Biconic vehicle: Pitch moment coefficient, C_m

the static trim angle is 26 degrees and at this value of α the L/D ratio is 1.0. Figure 7 illustrated the effect of the pitch/yaw moment coefficients in the (y_W, z_W) plane. The pitch moment coefficient, C_m , is illustrated as a function of α in Figure 9.

Figure 9 makes it clear that $\alpha = 0$ and $\alpha = 26$ are both equilibria; $C_m = 0$ for these values of α . However, only $\alpha = 26$ is stable as the slope of C_m is negative for this value of α .

3.2 Circular Symmetry Issues

The circular symmetry of the vehicle enables us to use a more intuitive coordinate system for the lift/yaw force coefficients. We will define a “lift direction angle,” θ_N , as the angle of the net lift/yaw force with respect to the vehicle vertical. We will also define an “effective angle-of-attack” α_e , as the angle-of-attack with respect to this angular direction (cf. α which is defined with respect to the vehicle vertical direction).

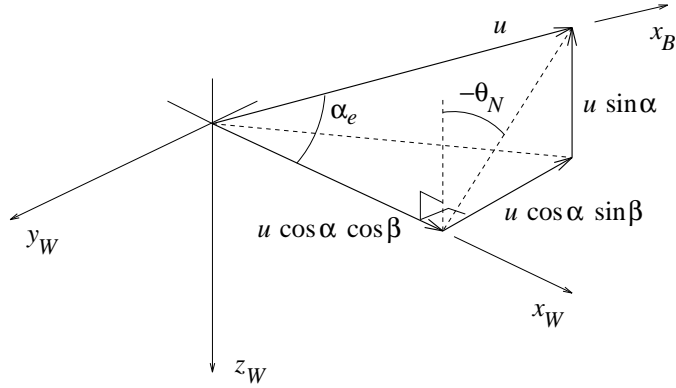


Figure 10: Definition of α_e (effective angle of attack) and θ_N (lift vector angle)

3.2.1 Definition of α_e and θ_N

A geometric illustration of α_e is given in Figure 10. It is the angle between the velocity vector and the x_B axis.

The components of the vector,

$$\mathcal{L}_{WB} \begin{bmatrix} u \\ 0 \\ 0 \end{bmatrix},$$

are the projection of u on the wind axes. These are shown in Figure 10, and it can be seen that α_e satisfies,

$$u \cos \alpha_e = u \cos \alpha \cos \beta.$$

Therefore, α_e (in the range $-\pi/2 < \alpha_e < \pi/2$), can be defined by,

$$\cos \alpha_e = \cos \alpha \cos \beta.$$

For small α and β , the total angle-of-attack,

$$\alpha_T := (\alpha^2 + \beta^2)^{1/2},$$

is good approximation to α_e . The total angle-of-attack is used by Spencer and Braun in their analysis of the Pathfinder trajectory [10]. The biconic vehicle exhibits significantly larger angles and so we will use the more exact α_e in the analysis.

The lift vector angle with respect to the body vertical direction, θ_N , is also illustrated in Figure 10. The bank angle, ϕ , is defined as the angle between the local vertical axis, z_V , and the body vertical axis, z_B , in the clockwise direction when viewed from the *rear* of the vehicle. We will define θ_N in the same manner, which gives the depiction of $-\theta_N$ in Figure 10. Note that the views depicted in Figures 6 and 7 are from the *front* of the vehicle.

Figure 10 illustrates that θ_N satisfies,

$$\tan(-\theta_N) = \frac{u \cos \alpha \sin \beta}{u \sin \alpha},$$

which implies that θ_N (in the range $-\pi < \theta_N < \pi$) can be defined by,

$$\tan \theta_N = \frac{-\cos \alpha \sin \beta}{\sin \alpha}.$$

Figure 10 also gives the good illustration of the reason for the choice of axes in Figures 3, 4, 6, and 7. In these plots the origin is on the x_W axis and the view is in the $-x_W$ direction. The (x,y) coordinate location of the vehicle nose is therefore given by $(\cos \alpha \sin \beta, \sin \alpha)$.

3.2.2 Bank angle and lift direction relationships

Previous aerodynamic re-entry control work has used bank angle modulation as a control parameter [1]. A similar approach will be applied here, although we must first use the definitions of the previous section to account for the combined lift and side forces in the control. Figure 11 illustrates the forces in question, from the point of view of the rear of the vehicle.

We define ϕ_N as the angle between the local vertical and the effective lift vector. Note that,

$$\phi_N = \phi_W + \theta_N, \tag{1}$$

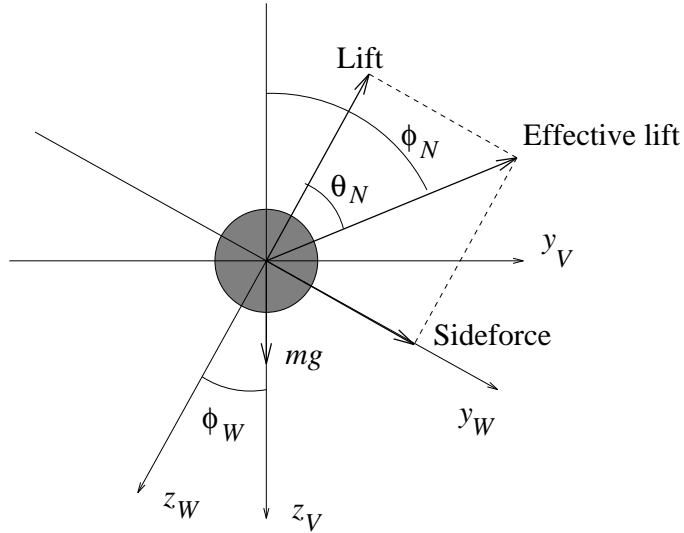


Figure 11: Normal forces acting on a circularly symmetric vehicle, viewed from the rear (sideforce acts in the $-y_W$ direction; vector shown is negative)

where ϕ_W is the bank angle of the wind frame. In the case where the sideslip angle (β) is zero, θ_N is also zero and bank angle modulation moves the lift vector as expected. For a biconic vehicle, the existence of the circle of static pitch/yaw equilibria at $\alpha_e = 26$ degrees means that β may be large and we must explicitly account for the side force component of the effective lift vector.

We therefore want to apply a modulation control strategy to ϕ_N . This is addressed in Section 5.

4 Ballistic Trajectory Analysis

The ballistic entry trajectory is calculated from a specified set of atmospheric entry conditions. The following nominal conditions are specified by Spencer and Braun [10] for the Pathfinder mission.

Latitude	22.9840	degrees
Longitude	338.9036	degrees
Radius from planet center	3522.2	km
Altitude	125.0	km
Velocity (km/sec)	7.350	km/second
Flight path angle, γ_W	-14.2	degrees
Azimuth (heading) angle, ψ_W	253.0995	degrees

The velocity can be controlled very accurately. Navigation and guidance errors in the interplanetary cruise phase cause errors in the other atmospheric entry parameters. We will look at errors in the flight path and azimuth angles (γ_W and ψ_W).

4.1 Nominal entry characteristics

Figures 13, 12, 14, 15, and 16 illustrate the results of a nominal Pathfinder entry trajectory using the above atmospheric entry initial conditions.

These results agree qualitatively with those presented by Spencer and Braun [10]. Their simulation contained significantly more detail of the planet (atmospheric and gravitational variations) and a more detailed map of the aerodynamic coefficients, particularly at low velocities.

Figure 15 illustrates the effective angle-of-attack. Note the high frequency oscillations which vary with the dynamic pressure. These are also evident in the total angle of attack given in [10]. The more detailed aerodynamic coefficient model in [10] also shows regions of local dynamic instability.

The peak dynamic pressure, shown in Figure 16, is 10,300 kg/m/sec². The drag force has a very similar shape and peaks at approximately 91,300 N at 69 seconds after entry. For comparison, the lift force is oscillatory and reaches a peak value of only 7.7 N. This is not surprising as α_e is very small throughout the trajectory.

The terminal conditions, just above the planet surface, are given below.

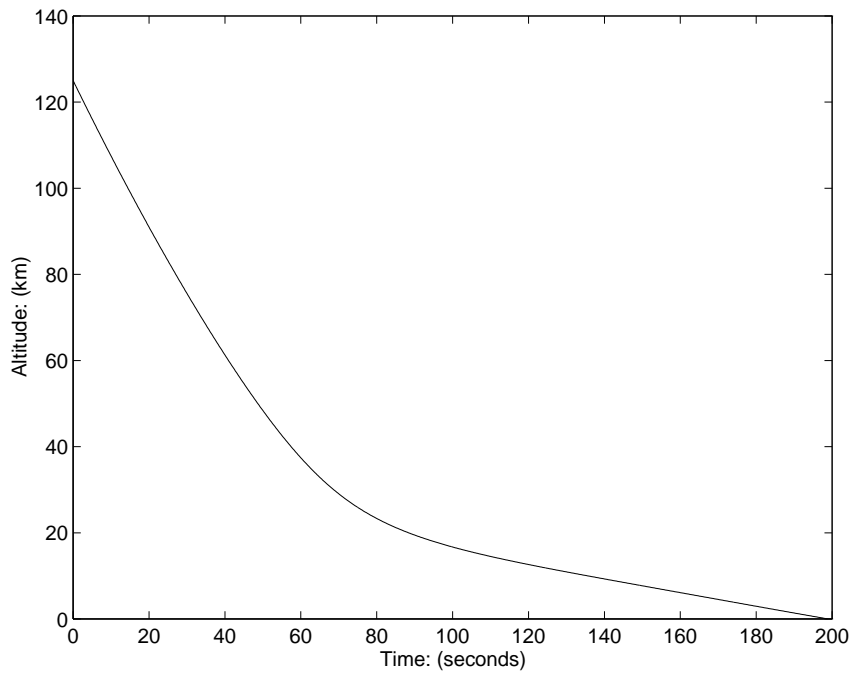


Figure 12: Pathfinder nominal entry (altitude vs. time)

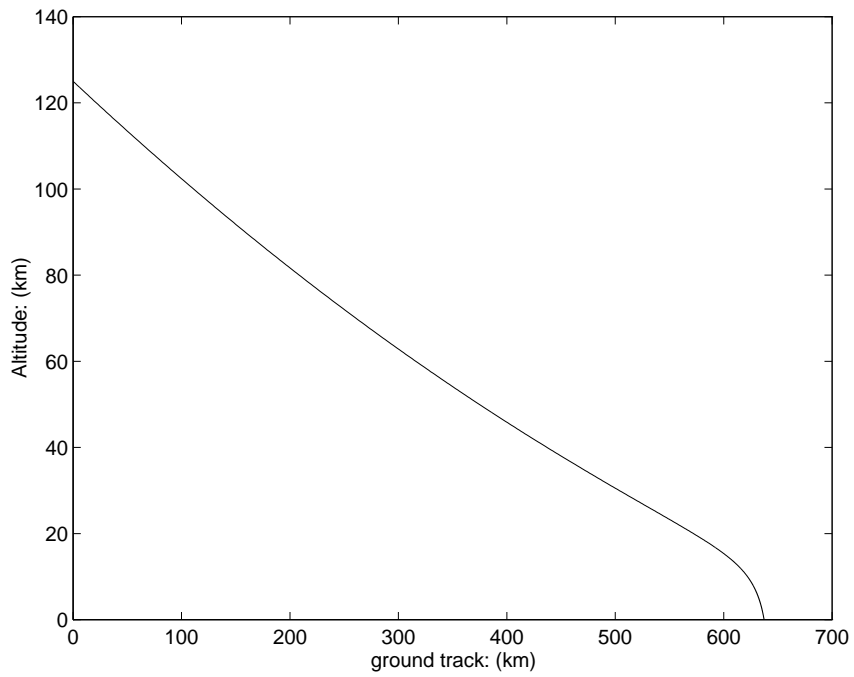


Figure 13: Pathfinder nominal entry (altitude vs. ground track distance)

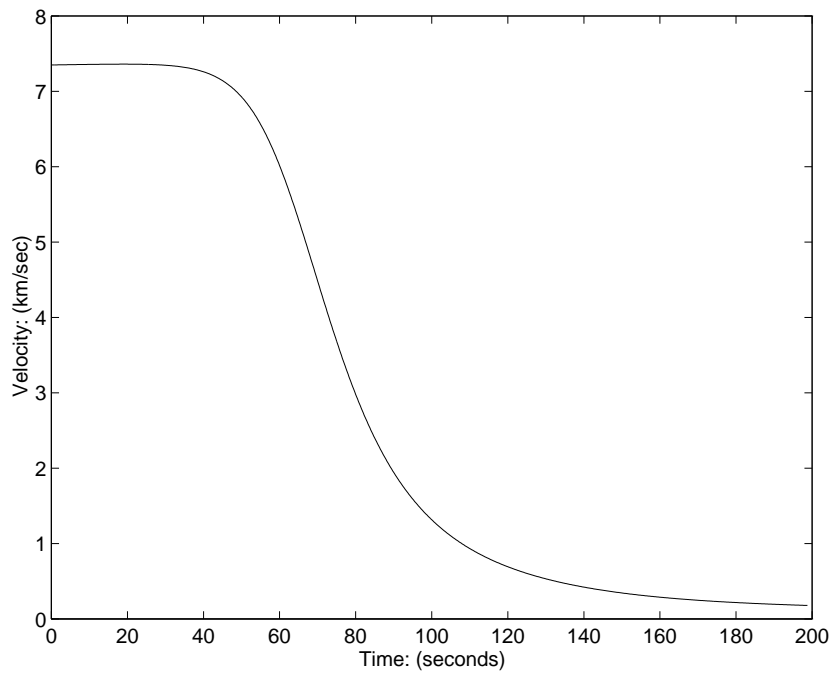


Figure 14: Pathfinder nominal entry (velocity profile)

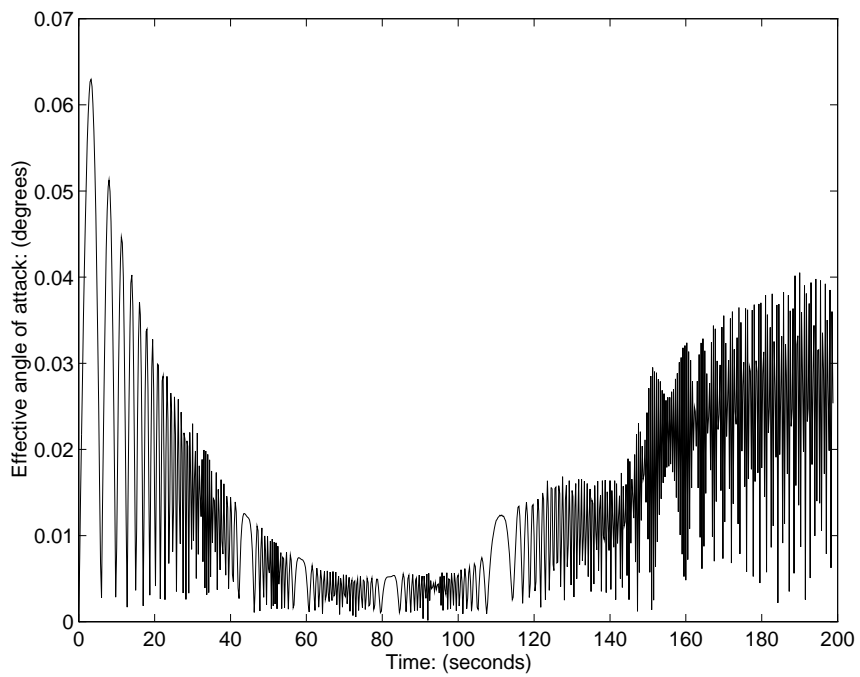


Figure 15: Pathfinder nominal entry (effective angle-of-attack, α_e)

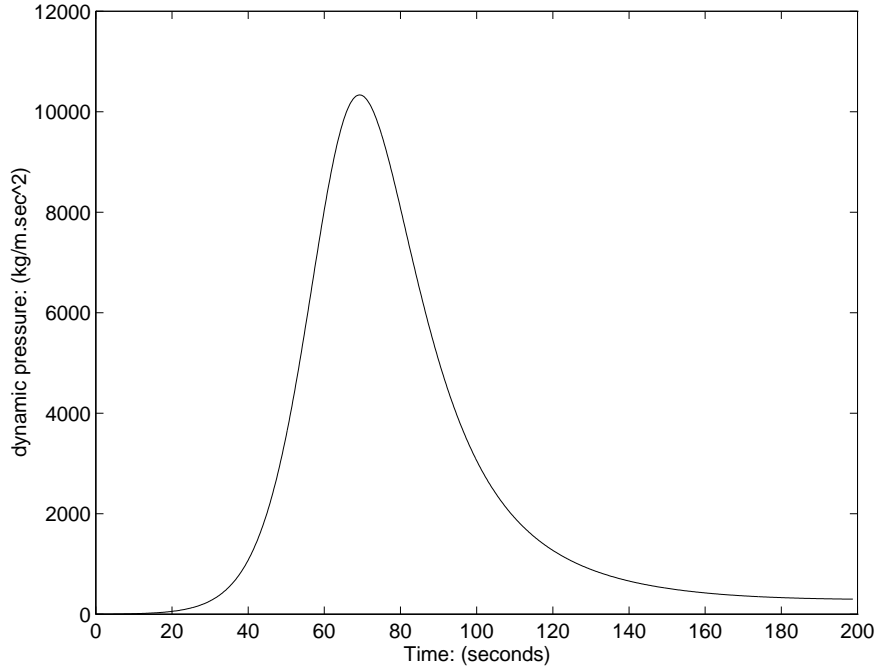


Figure 16: Pathfinder nominal entry (dynamic pressure)

Time from atmospheric entry	198.75	seconds
Velocity	179.0	meters/second
Dynamic pressure	299.8	kg/m/sec ²
Altitude	26.6	meters
Flight path angle, γ_W	-58.7	degrees
Azimuth (heading) angle, ψ_W	243.7	degrees

The actual mission will deploy a parachute at approximately 8 km altitude. The trajectory terminal conditions given above are more for comparison with the lifting vehicle terminal conditions given in Section 5.

4.2 Analysis of flight path and azimuth errors

We consider variations in flight path angle, γ , and heading angle, ψ_W . The variations are circular and up to ± 1.0 degrees on each variable. This corresponds approximately to the 3σ error level in the Pathfinder mission. Figure 17 shows the resulting elliptical error envelope at an altitude of 15 km.

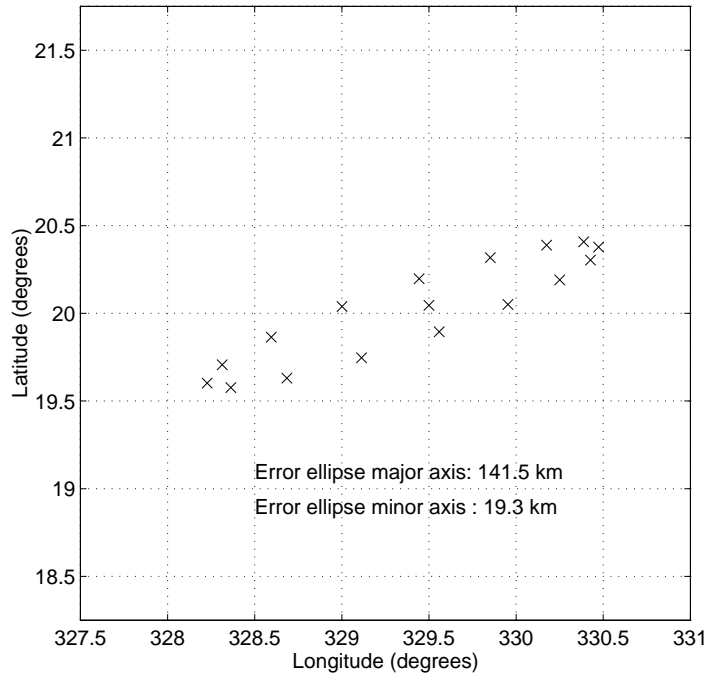


Figure 17: Pathfinder initial condition error analysis: $\gamma = -14.2 \pm 1.0$ degrees, $\psi_W = 253.1 \pm 1.0$ degrees

Note that errors in the flight path angle, γ , have a much greater effect. They account for the 141.5 km major axis in the error envelope. This error analysis did not consider any uncertainty in atmospheric density, winds, or aerodynamic properties.

Figure 18 illustrates the effect of errors in γ and the entry altitude on the trajectory. The total extent of the range error is now 173.4 km. Careful examination of the plot will show that errors in γ are again the most significant contribution.

The major axis of the error ellipse for the Pathfinder mission is 299 km [10]. The other major contributing factors are the atmospheric and aerodynamic uncertainties, which we do not consider in this initial analysis.

4.3 Control options for the ballistic vehicle

This target ellipse is large, with significant contributions from errors in the entry conditions and the atmospheric and aerodynamic uncertainties. Implementing an accurate landing strategy will require some form of aeromaneuvering control during the entry

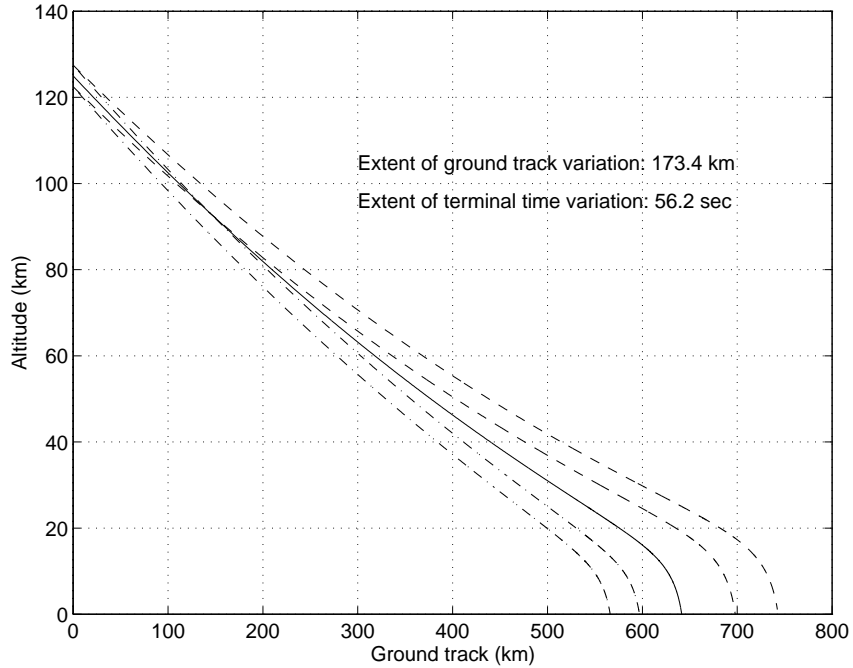


Figure 18: Pathfinder initial condition error analysis: $\gamma = -14.2 \pm 1.0$ degrees, entry altitude is 125.0 ± 2.5 km

phase.

The trim angle of this vehicle is $\alpha = 0$. In order to generate significant lift the vehicle must be flown at a large effective angle-of-attack, α_e . The slope value of the C_m coefficient at significant values of α , and the magnitude of the dynamic pressure, means that the torques required to fly the vehicle at significant angle-of-attack are orders of magnitude beyond what is available from thrusters.

The only means of obtaining significant lift is to change the trim value of α . This can be done by appending fins and/or aerodynamic control surfaces, or by shifting the vehicle center of mass. This has not yet been studied because there is no aerodynamic data base available for the simulation.

A vehicle configuration like Pathfinder has significant packaging advantages. Modifications such as a center of mass shift are likely to result in an L/D ratio of only 0.3. It is still a research issue as to whether this is sufficient to allow for closed-loop compensation for the errors described in the previous section. See Section 6.2 for an outline of the future research issues.

5 Controlled Lifting Vehicles

We now consider a controlled descent for the biconic lifting vehicle detailed in Section 3.1.2. A simple control system was designed and simulated to investigate the closed-loop tracking capabilities of the vehicle. This approach should be considered as preliminary and is only used to gain a rough idea of vehicle capabilities.

The control approach described in the subsequent sections can be considered as a form of bank angle control. This type of control is also used for the Shuttle re-entry trajectory.

5.1 Directional Targeting Approaches

A nonlinear attitude controller was designed to allow control of the vehicle bank angle. This effectively gives the control system the ability to point the aerodynamic lift vector in a specified direction.

The simulation assumed that the controller had knowledge of the current vehicle position and attitude, and the target position. The effect of errors in the control system knowledge will be investigated at a later date.

For the purposes of the simulation control is effected via roll, pitch and yaw thrusters. In practice, aerodynamic fins and/or center of mass motions may be more efficient and more effective.

5.1.1 Control of ϕ_N

The vehicle will be maneuvered by controlling the angle of the lift vector with respect to the local vertical, i.e. ϕ_N . Recall from (1) that this is given by,

$$\phi_N = \phi_W + \theta_N.$$

Lower level controllers, described below, will be used to control ϕ_W (bank angle control) and θ_N (lift vector angle control).

Note that at the trim value of the effective angle-of-attack (α_e) the lift/side force vector is similar in magnitude to the drag force. During the region of maximum dynamic

pressure it is significantly larger than the gravitational force. The definition of ϕ_N can be interpreted as follows.

$$\phi_N = \begin{cases} -90 & \text{degrees: turn to the left} \\ 0 & \text{degrees: pull up} \\ 90 & \text{degrees: turn to the right} \end{cases}$$

The pitching moment coefficient, C_m , has a large enough slope that the restoring torques keep α_e close to its trim angle (approx. 26 degrees) for most flight conditions. The only exception is at the start of the flight when the atmospheric density is very low.

The lift/side forces are such that if ϕ_N remains within ± 75 degrees (approx.) the vehicle will skip out of the atmosphere. This means that the controller must maintain ϕ_N around ± 90 degrees—which means that it must effectively flip the lift/side force vector from side to side. The restoring pitching torques are such that in moving from one side to the other, the vehicle nose must rotate through the pitch up position ($\phi_N = 0$). This means that a side to side transition will also provide vertical lift as the vehicle nose rotates.

The two variables we will consider controlling are trajectory range and direction. To steer the vehicle to the left ϕ_N is held in the range -85 to -110 degrees. Similarly to steer it to the right, $85 \text{ deg.} \leq \phi_N \leq 110 \text{ deg.}$ The course direction is controlled by modulating between these two conditions. The range can be controlled by specifying ϕ_N between the switches. Clearly if $\phi_N = 85$ degrees there is a vertical lift component which extends the vehicle range. If $\phi_N = 110$ degrees the vertical lift component is in the downward direction and the range is shortened.

To make this more precise, define ϕ_{Nlimit} as the magnitude of the steady value of ϕ_N when not switching. Recall that ψ is the velocity vector azimuth, and define ψ_T as the vector from the vehicle to the target. The following basic algorithm generates a reference, ϕ_{Nref} for tracking by the lift control algorithm (described in Section 5.2.2).

We define a switching signal, $\phi_{Nswitch}$, by the following.

```

If ( $\psi_t - \psi$ ) > 1.0 degrees
     $\phi_{Nswitch} = \phi_{Nlimit}$  (turn to left)
elseif ( $\psi_t - \psi$ ) < -1.0 degrees
     $\phi_{Nswitch} = -\phi_{Nlimit}$  (turn to right)
else
    maintain same value of  $\phi_{Nswitch}$ 

```

endIf

This has the effect of switching the turn direction to the opposite side when the directional error to the target exceeds 1.0 degrees.

When the altitude was less than 10 km, ϕ_{Nlimit} was set to 10 degrees. This results in the majority of the lift/side force being applied vertically, which has the effect of flaring out the final approach and further slowing the vehicle.

The tracking reference for the lower level controllers was generating by passing $\phi_{Nswitch}$ through a smoothing filter. The dynamics of this filter were given by,

$$\phi_{Nref} = \frac{2}{s^2 + 3s + 2} \phi_{Nswitch}.$$

Using smooth transitions in ϕ_{Nref} reduced the size of the transient control actuation commands in the lower level attitude controllers.

5.2 Attitude Control

We shall proceed by using the roll thruster to regulate ϕ_W (the bank angle) to zero. Lift vector control is then implemented by regulating θ_N to the ϕ_N reference value: ϕ_{Nref} . This approach, and the algorithms used to implement it, should be viewed only as an initial method. A more detailed study of optimal and/or robust attitude controllers are left as future research (see Section 6.2).

5.2.1 Bank angle control

The bank angle dynamics are given by,

$$\begin{aligned} \dot{\phi}_W &= p + q\phi_W \tan \theta + r(1 - \phi_W) \tan \theta \\ &= \phi_W \tan \theta (q - r) + p + r \tan \theta. \end{aligned} \quad (2)$$

Define a reference roll rate, p_{ref} , by

$$p_{ref} = -\phi_W - q \sin \phi_W \tan \theta - \cos \phi_W \tan \theta r. \quad (3)$$

Substituting (3) into (2) gives,

$$\dot{\phi}_W = -\phi_W + (p - p_{ref}).$$

Now a simple roll controller which gives, $p \approx p_{ref}$, will give,

$$\dot{\phi}_W \approx -\phi_W,$$

and ϕ_W will be driven to zero. If we neglect the crossterms in the inertia matrix, the roll dynamics are given by,

$$\dot{p} = I_x^{-1}L,$$

where L is the applied roll moment. Proportional control is the simplest means of driving p to p_{ref} . The control moment to be applied is given by,

$$L = K_p I_x (p_{ref} - p),$$

where p_{ref} is calculated from (3) via measurements of ϕ_W , q , r , and θ . In the simulations below, the proportional gain was selected, by several simulations, to be $K_p = 40$. This controller has been found to keep ϕ_W to typically within ± 0.2 degrees for straight trajectories. Large turning maneuvers result in larger deviations but the control does make ϕ_W small compared to θ_N .

The noise and parameters sensitivity, as well as other robustness aspects, of this controller have yet to be investigated.

5.2.2 Lift vector control

We now proceed to define a controller for ϕ_N under the assumption that $\phi_W = 0$. This amounts to controlling θ_N . We will follow a similar approach to Section 5.2.1 and define the control in terms of reference pitch and yaw rates (q_{ref} and r_{ref}).

Controlling θ_N is accomplished by moving the vehicle nose around the stable equilibrium circle illustrated in Figure 7. Figure 19 illustrates the angular direction for application

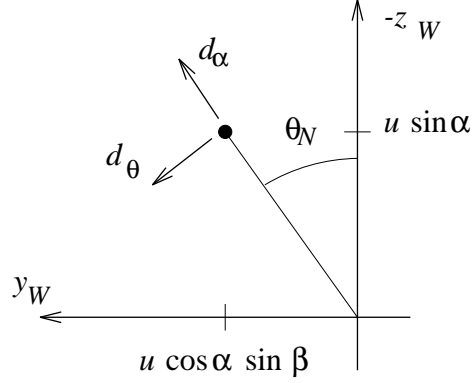


Figure 19: Radial and tangential velocity vectors (d_α and d_θ) definitions for the lift vector control problem

of the control torque. This view is from the x_W axis, where the solid dot denotes the nose of the vehicle.

The pitch and yaw rates affect α and β (or more precisely, $\sin \alpha$ and $\cos \alpha \sin \beta$) in the following manner.

$$\begin{aligned} q &\approx \dot{\alpha} \approx \frac{d \sin \alpha}{dt}, \\ r &\approx \dot{\beta} \approx \frac{d \cos \alpha \sin \beta}{dt}. \end{aligned}$$

Define d_θ and d_α as the derivatives of the position of the nose in the tangential and radial directions respectively (as illustrated in Figure 19). We can then relate these to the pitch and yaw as follows.

$$\begin{bmatrix} d_\theta \\ d_\alpha \end{bmatrix} = \begin{bmatrix} \cos \theta_N & -\sin \theta_N \\ \sin \theta_N & \cos \theta_N \end{bmatrix} \begin{bmatrix} r \\ q \end{bmatrix}. \quad (4)$$

For effective control we would like to apply torques such that $d_\alpha = 0$ and d_θ is the desired value for $\dot{\theta}_N$.

The assumption that $\phi_W \approx 0$ is enforced by the roll controller given above (Section 5.2.1), which means we can choose,

$$\theta_{Nref} = \phi_{Nref},$$

where ϕ_{Nref} is the reference lift vector angle, calculated by the control approach outlined in Section 5.1.1.

Now consider a simple gain-scheduled proportional controller, designed to track a specified lift vector angle, θ_{Nref} .

$$d_{\theta_{ref}} = -K_{\theta}(\theta_{Nref} - \theta_N).$$

This specifies a velocity, in the d_{θ} direction, which is proportional to the error between θ_{Nref} and the actual angle, θ_N . This can be expressed in terms of reference pitch and yaw rates (q_{ref} and r_{ref} respectively) by inverting (4).

$$\begin{aligned} q_{ref} &= \sin \theta_N d_{\theta_{ref}}, \\ r_{ref} &= -\cos \theta_N d_{\theta_{ref}}. \end{aligned}$$

Now a lower level scheme is used to track the reference pitch and yaw rates. We use a proportional controller, with a nonlinear correction for the inertia crossterms. The pitch and yaw torques (M and N) are given by,

$$M = -r_y(I_z - I_x)rp + r_y I_y K_q (q_{ref} - q), \quad (5)$$

$$N = -r_z(I_x - I_y)pq + r_z I_z K_r (r_{ref} - r), \quad (6)$$

where r_y and r_z are the pitch and yaw moment arms respectively.

Several preliminary simulations have been used to select values for the proportional gains. In the pitch/yaw control the choices are,

$$\begin{aligned} K_q &= 1.0 \\ K_r &= 1.0 \end{aligned}$$

It has been found to be necessary to reduce the gain in the θ_N control loop to prevent excessive overshoot at higher altitude flight conditions (where the control forces are significant compared to the aerodynamic restoring torques). The following gain was used in subsequent simulations.

$$K_{\theta} = \begin{cases} 0.3 & \text{for altitudes} \leq 60.0 \text{ km} \\ 0.06 & \text{for altitudes} > 60.0 \text{ km} \end{cases}$$

5.3 Preliminary Simulation Results

In each of the subsequent simulations the following nominal entry conditions were used.

Latitude	22.9840	degrees
Longitude	338.9036	degrees
Radius from planet center	3592.2	km
Altitude	195.0	km
Velocity (km/sec)	5.500	km/second
Flight path angle, γ_W	-14.0	degrees
Azimuth (heading) angle, ψ_W	253.0995	degrees

5.3.1 Directional tracking study

An simple control scheme was simulated to investigate the issue of control system authority during atmospheric entry.

The algorithm, outlined in Section 5.1.1, consisted of switching the bank angle whenever the angular difference between the velocity vector and the direction to target exceeded one degree. A simulation illustrated that this simple control system was able to keep the directional error to within one degree.

Figure 20 illustrates the resulting 2-D groundtrack. The vehicle executes a lefthand turn to align the trajectory with the target. Note that the maximum control effectiveness occurs at 327 degrees longitude and 19 degrees latitude. At this point the vehicle is experiencing maximum dynamic pressure (approximately 3,400 kg/m/sec²).

The trajectory is given in more detail in Figures 21 and 22. Note that the controlled, lifting trajectory is significantly longer in duration than the ballistic entry trajectory.

The velocity profile is illustrated in Figure 23.

The terminal conditions, just above the planet surface, are given below.

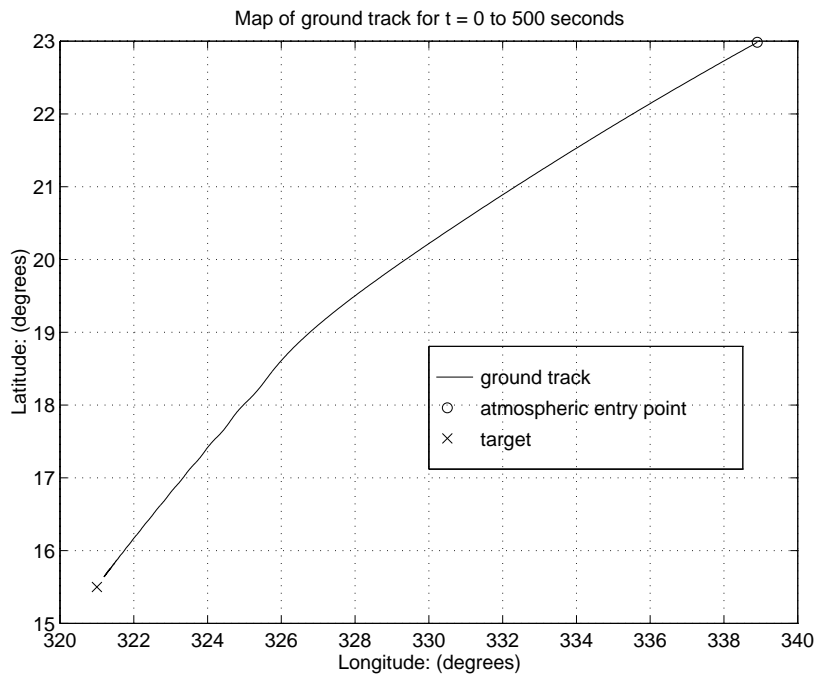


Figure 20: Lifting vehicle controlled entry: 2-D groundtrack

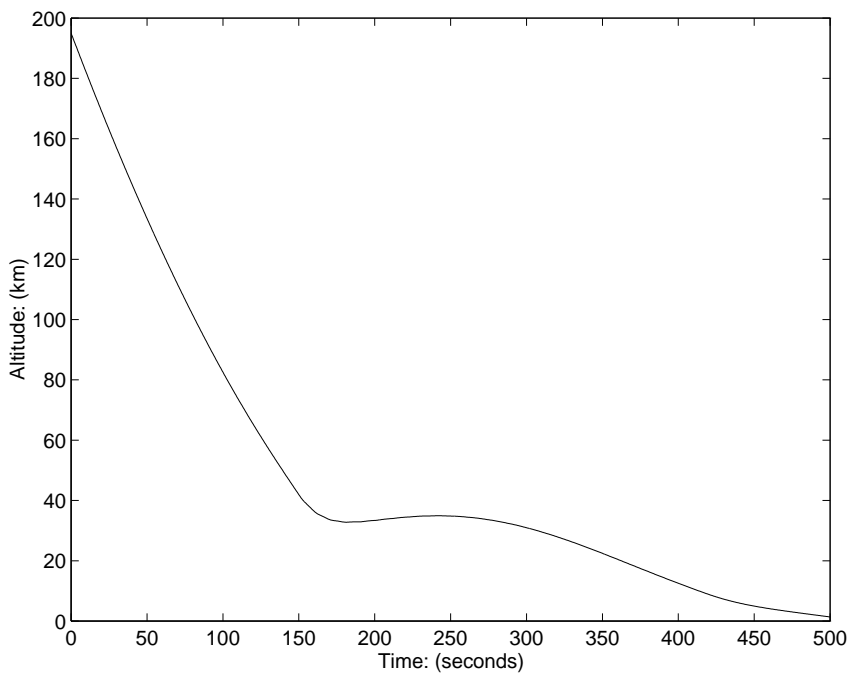


Figure 21: Lifting vehicle controlled entry: altitude/time profile

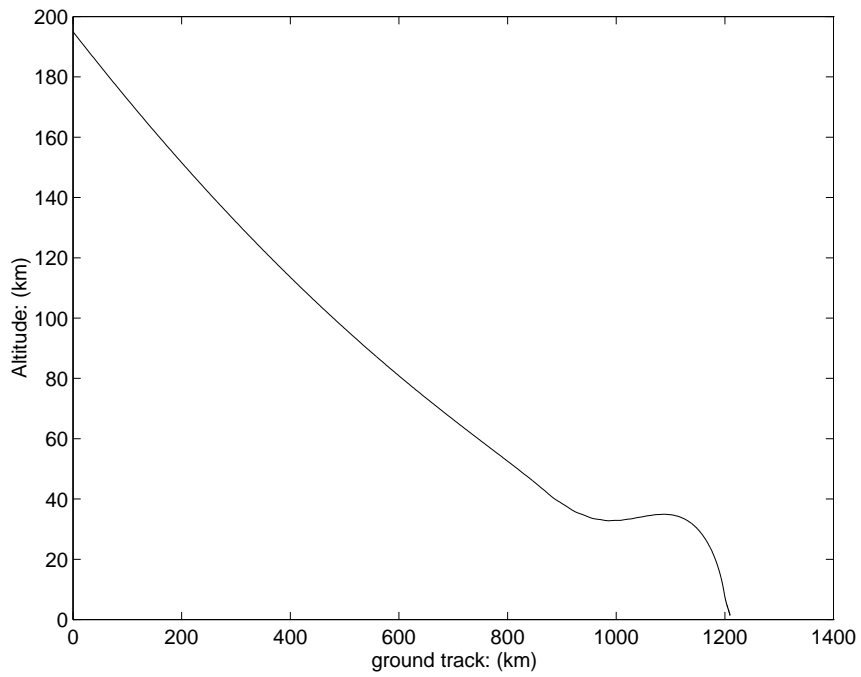


Figure 22: Lifting vehicle controlled entry: altitude/groundtrack profile

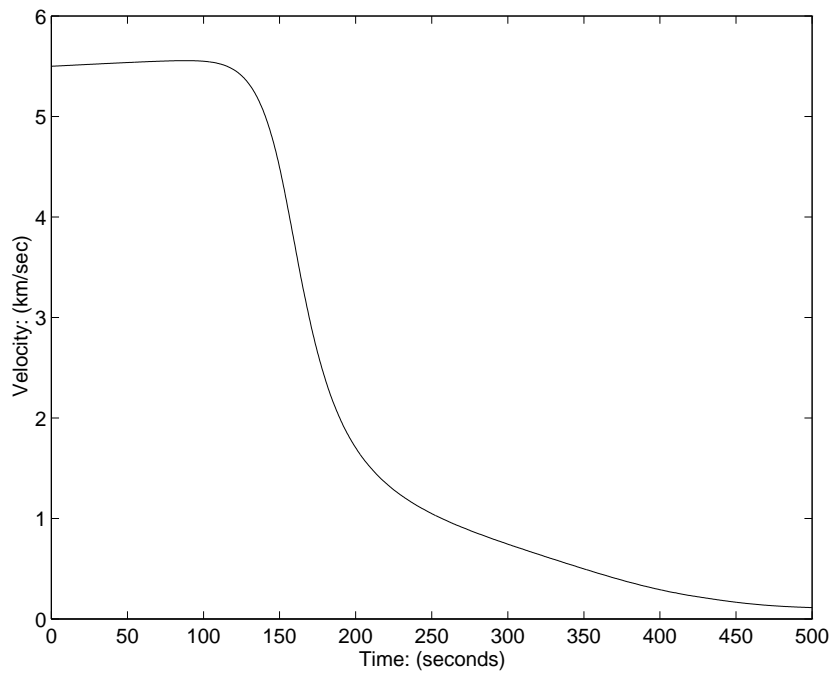


Figure 23: Lifting vehicle controlled entry: velocity profile

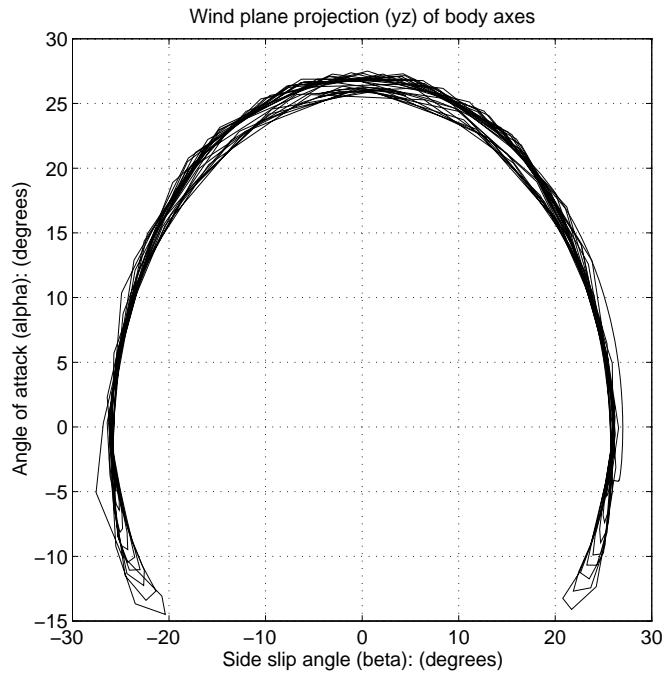


Figure 24: Lifting vehicle controlled entry: vehicle aerodynamic angles

Time from atmospheric entry	509.0	seconds
Velocity	106.1	meters/second
Dynamic pressure	105.6	kg/m/sec ²
Altitude	0.4	meters
Flight path angle, γ_W	-39.3	degrees
Azimuth (heading) angle, ψ_W	235.61	degrees

Note that the lifting vehicle is significantly slower than the ballistic vehicle at this point above the surface.

The basic method of control can be seen in Figure 24, which illustrates the locus of the vehicle nose (viewed from the front) with respect to the velocity vector. This illustrates that the vehicle is banking through an angle of approximately 210 degrees. The banking occurs around the trim angle-of-attack of 26 degrees. A full 6-DOF simulation is used to capture the effect of bank angle modulation on the vertical lift force.

The effect of these bank angle maneuvers on the side force vector is shown in Figure 25. The lateral modulation of the side force vector enables the vehicle to be steered. Each transition occurs when the direction error exceeds one degree. Note that effective control

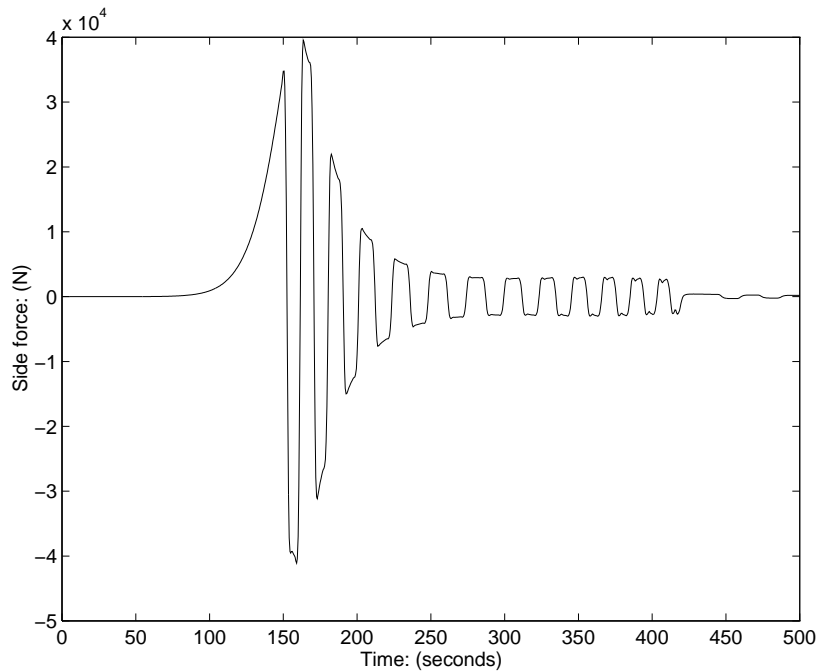


Figure 25: Lifting vehicle controlled entry: side forces

is maintain from 140 seconds onwards.

The lift force vector is illustrated in Figure 26. Note that the banking maneuver gives significant lift during the side to side transitions. Note also that some of the lift is negative—the vehicle attitude gives an aerodynamic downward force. Controlling the relative ratio of the upwards/downwards forces during this maneuver will enable control of the length of the groundtrack. This has not yet been investigated.

In contrast to the ballistic case, the side forces are of a similar magnitude to the lift forces. Both forces significantly exceed gravity for the majority of the flight time. This large side force (available via vehicle attitude control) gives an effective means of steering the vehicle.

5.3.2 Range authority study

The earlier ballistic vehicle studies indicated that the flight path angle error is one of the most significant factors in the size of the final target area ellipse. This issue has also been investigated for the controlled lifting vehicle.

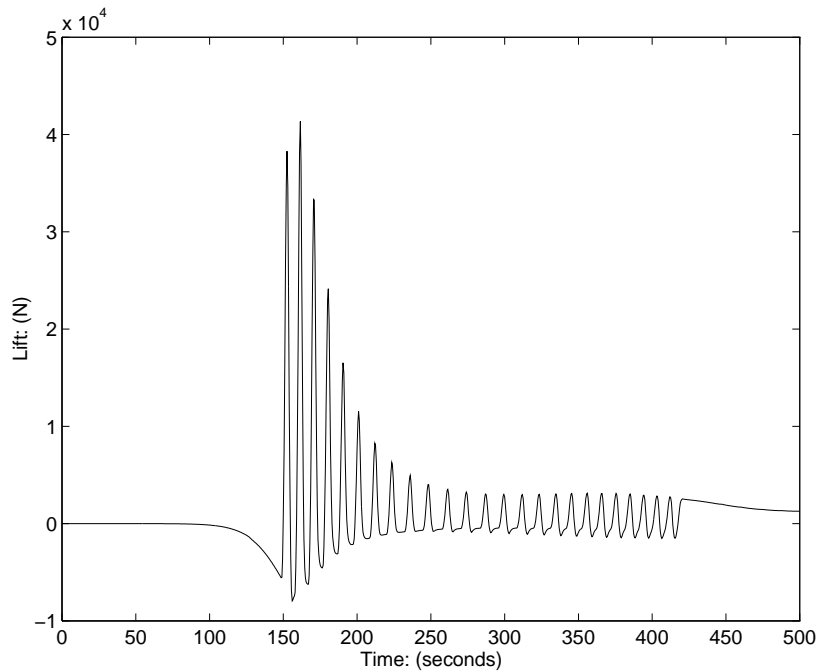


Figure 26: Lifting vehicle controlled entry: lift forces

Simulations were run using a nominal lift vector angle switching angle of $\phi_{Nlimit} = 90$ degrees. The reference lift vector angle was fixed as a 50 seconds square wave rather than being driven by a directional control algorithm. Figure 27 illustrates the 2-D groundtrack which results from $\gamma = -13.0, -14.0,$ and -15.0 .

The resulting terminal conditions are given in the table below.

Flight path angle γ (deg.)	Flight time (seconds)	Latitude (deg.)	Longitude (deg.)	Velocity m/sec
-13.0	662.0	13.83	313.96	107.0
-14.0	564.5	16.06	318.98	106.9
-15.0	505.5	17.00	321.92	106.7

The total range of the resulting ground track is 535.4 km. Due to the lifting nature of the trajectory this is significantly larger than the flight path error target deviation in the ballistic case. Figure 28 illustrates the altitude versus groundtrack profile for each of the cases discussed above.

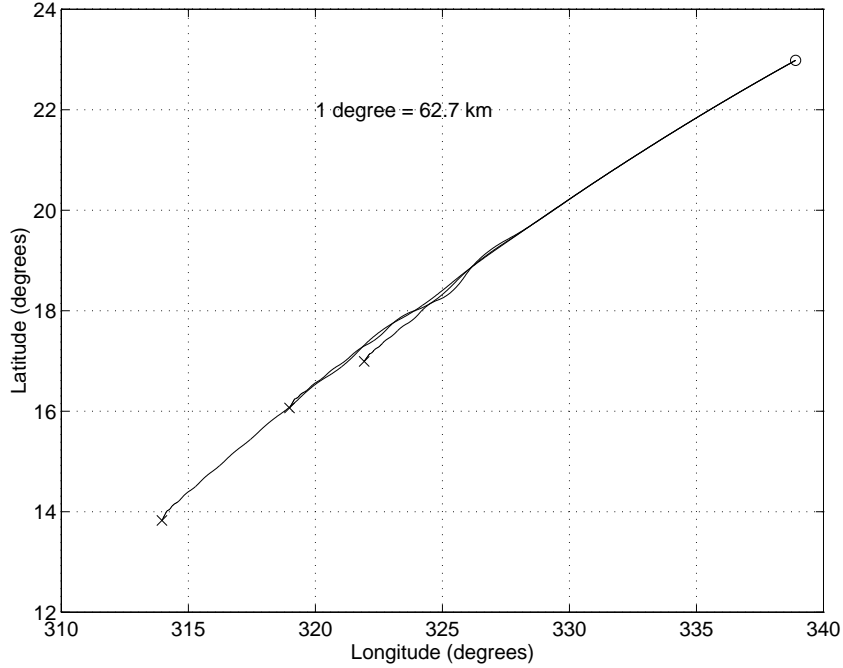


Figure 27: Flight path angle error groundtrack comparison for the biconic vehicle. $\gamma = -14.0 \pm 1.0$ degrees. Nominal lift vector angle, $\phi_{Nlimit} = \pm 90$ degrees

Note that the flight path error causes a deviation in the trajectories, even at high altitudes. The issue to be studied is whether control of the lift vector angle can be used to compensate for the flight path angle errors. This capability is studied by simulating period switching trajectories (again using a 50 second period giving 25 seconds per side) for $\phi_{Nlimit} = 85, 90, 100,$ and 110 degrees. The 2-D groundtrack of these simulations is illustrated in Figure 29.

The terminal conditions are again tabulated below. In this case $\gamma = -14.0$ degrees for all simulations.

Lift vector angle limit ϕ_{Nlimit} (deg.)	Flight time (seconds)	Latitude (deg.)	Longitude (deg.)	Velocity m/sec
85	705.0	14.21	314.71	107.5
90	564.5	16.06	318.98	106.9
100	466.5	16.94	321.10	106.8
110	362.5	17.82	322.96	111.9

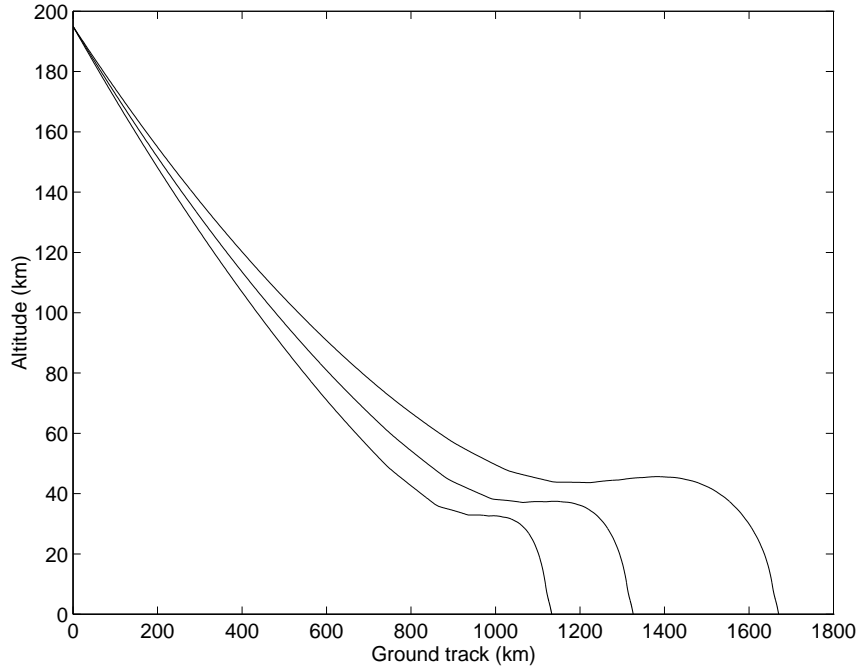


Figure 28: Flight path angle error comparison (altitude vs. groundtrack) for the biconic vehicle. $\gamma = -14.0 \pm 1.0$ degrees. Nominal lift vector angle, $\phi_{Nlimit} = \pm 90$ degrees

The total ground track range, achievable via control of ϕ_{Nlimit} , is 562.9 km. This is enough to compensate for the errors which result from a ± 1.0 degree error in γ . Figure 30 shows the altitude versus ground track profile for each case. Note that they differ only for altitudes less than 60 km.

6 Research Issues

6.1 A Summary of the Results

The Pathfinder simulations illustrated that azimuth and flight path angle errors lead to a significant error ellipse (140×20 km) at the planet surface. Atmospheric and aerodynamic uncertainties will cause further significant increases in the error ellipse.

Closed-loop control of a lifting vehicle has been studied for the precision landing problem. A hierarchical scheme, involving attitude control, and bank angle control, has been studied to investigate control authority issues.

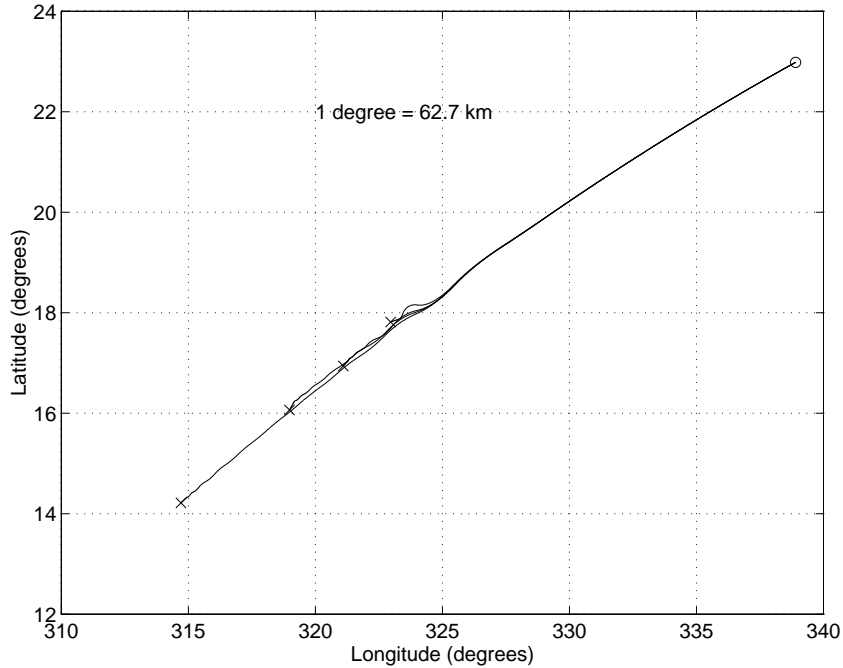


Figure 29: Range control capabilities of the biconic vehicle. $\phi_{Nlimit} = 85, 90, 100,$ and 110 degrees. 2-D groundtrack

An initial investigation illustrates that control of the lift vector angle has sufficient authority to correct for known flight path angle errors. Preliminary simulations also indicate that control of the lifting vehicle can be used for effective directional control. Directional accuracy of ± 1.0 degrees was easily achieved. The lifting body aeromaneuvering trajectories also show lower peak dynamic pressures, lower terminal velocities and longer flight times than ballistic trajectories.

6.2 Immediate Research Issues

The work described in this report should be considered as an initial investigation into the aeromaneuvering control problem. A further and more complete investigation is required in certain areas, and various control research issues immediately arise. These items are discussed here. The next section outlines the longer term research areas.

Descent path control strategies. The work above used a nominal descent path, based largely on heuristics. A more precise study of the choice of this trajectory is re-

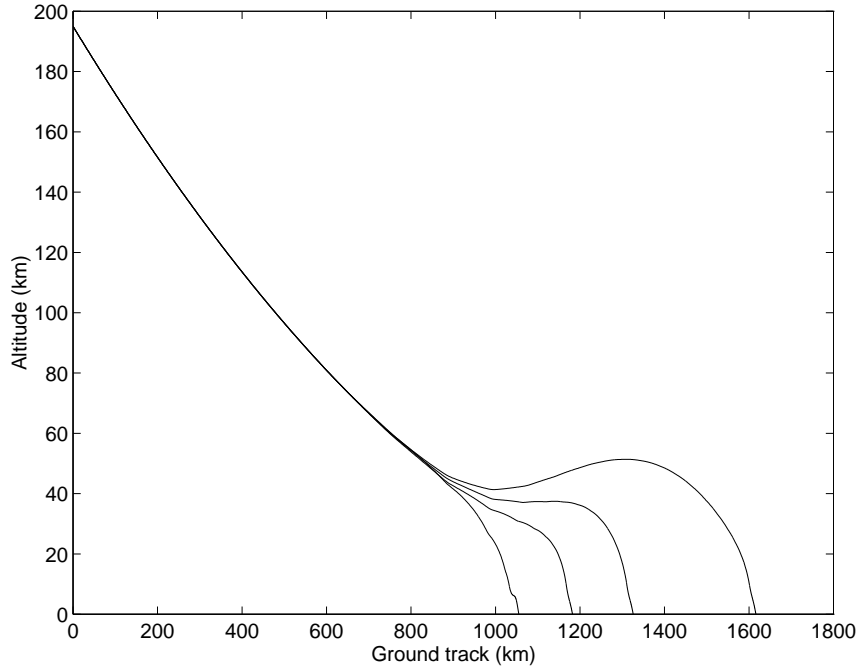


Figure 30: Range control capabilities of the biconic vehicle. $\phi_{Nlimit} = 85, 90, 100,$ and 110 degrees. Altitude vs. ground track

quired. This will involve studying the above descent path in more detail, as well as formulating the descent path selection problem in control relevant terms.

The relationship between the nominal descent path and the landing objectives (positional accuracy, velocity, and final attitude) should be quantified in greater detail and used to redesign the nominal descent path.

A study of the sensitivity of the nominal descent path with respect to initial navigation errors is required. The issue of the robustness of the path with respect to atmospheric uncertainties and vehicle aerodynamic uncertainties is a related and equally important issue.

Attitude control. A relatively simple attitude control system was simulated in Section 5. This area requires a more systematic investigation.

The lift vector angle approach, outlined in Section 5.1 should be investigated with respect to the effect of atmospheric and vehicle aerodynamic uncertainties. This aspect relates also to the descent path control strategies discussed above. The lift vector angle control strategy will also influence the achievable range.

The local loop attitude controllers described in Sections 5.2.1 and 5.2.2 were based on hierarchical proportional controllers with nonlinear correction terms. While this

gave adequate results in the nominal case, there was no attempt at a systematic design to account for the effects of dynamic uncertainty. This issue must be studied in greater detail. Several approaches could lead to more systematic control designs. The first of these is a nonlinear inversion approach. This involves the design of dynamic inverting controllers for some parts of the vehicle dynamics. Such controllers will be applied selectively in order to maintain any beneficial nonlinear effects. This approach is being studied for high performance aircraft problems [11]. There is a trade-off between the degree of inversion achieved, and the sensitivity of the system to uncertainty. This trade-off requires further study.

The aerodynamic forces vary through several orders of magnitude during the controlled region of the descent path trajectory. A second, and complementary, approach involves the application of gain scheduling, based on dynamic pressure. The large variations in control effectiveness and vehicle response can be handled in a systematic manner. The controllers in Section 5 already do this to a very limited extent by switching some of the proportional gains as a function of altitude. A more systematic approach would give significant benefits.

Vehicle redesign and control options. The lifting vehicle studied here is not particularly well suited to a small landing mission. The vehicle characteristics should be modified to be more in line with current mission requirements. This will involve redeveloping an aerodynamic database for the modified vehicle.

Part of this effort will include the study of alternative actuation mechanisms. Aerodynamic fins and/or center of mass actuators would provide more efficient aerodynamic actuation. This will involve modifying the aerodynamic database as well as the simulation. Center of mass modifications are relatively straightforward. Including aerodynamic control surfaces is more complex and should be considered as a longer term research item.

Noise and uncertainty issues. The simulations described in this report for the large part involve nominal conditions. The simulation functions should be modified to allow for the inclusion of sensor noise and dynamic system uncertainties. This will give a more realistic basis for the control system designs.

6.3 Longer Term Research Areas

The previous section dealt with short term research problems resulting from the initial work described in this report. We now look at the longer term research items in order to provide some context for the discussion in the previous section.

Landing objective control strategies. The overall objective is the closed-loop tracking of the descent path. The relationship between the local path tracking error and the resulting landing error is nonlinear and needs a detailed study. A more precise quantification of landing errors is required. The landing precision will impose performance requirements on the subordinate control systems.

The hierarchical control strategy requires further consideration. We can postulate the following illustrative hierarchy.

1. Target selection/reselection based on sensed information and science requirements.
2. On-board descent path determination. This will involve selecting trajectories on the basis of the sensitivity and performance trade-off.
3. Path tracking algorithms. A preliminary version has been considered in this report.
4. State estimation and attitude control.
 - 4a. System estimation algorithms. An adaptive characterization of system noise and/or environmental variables may be required.
 - 4b. Attitude control systems. Again preliminary versions have been considered in this report.
5. Sensing and actuation.
 - 5a. Sensing systems. These may involve local control loops or local adaptive characterization of noise.
 - 5b. Actuation. Again local feedback loops will be required.

The interactive effects of errors and uncertainty between hierarchical levels will have a significant effect on the overall system performance. Note also that different levels may have different control implementations; there may be discrete-event or logic control, digital control, and local loop analog control running simultaneously.

Another issue, arising in the above, is the requirement for a multi-objective control scheme in which the priorities can change as a function of current (or predicted) spacecraft and environmental conditions. For example, the following objectives can be considered.

1. Thermal limit avoidance.
2. Dynamic pressure limit avoidance.
3. Terminal targeting performance.

4. Terminal attitude requirements.
5. Path tracking performance.

The terminal conditions in the controlled lifting body simulations allow an alternative landing scenario to be considered. It may be possible to consider landing without a parachute. In this case, as the vehicle approached the planet surface, the attitude control system would align the main thruster for the final deceleration and soft landing. This is a significant departure from the previously considered methods and would involve significant technological development.

Landing error quantification and technology trade-offs. The sensed information available will affect the final landing performance. There is a trade-off between the level of sensing and information infrastructure, and the system performance. For example, some or all of the following can be considered.

1. Inertial measurement unit.
2. Single altitude radar.
3. Doppler radar altitude/velocity sensing.
4. Planet based navigation beacons.
5. Orbiting beacon(s) or radio reference.
6. Aerodynamic angle-of-attack sensors.
7. Dynamic pressure sensor.
8. Optical target tracking.
9. Laser ranging.

Combinations of these scenarios will provide different levels of information. This must be studied from a landing objective performance point of view. Note that the study must include the effects of sensing and system uncertainty.

Aspects of this work require the concurrent development of actuation and sensing subsystem models.

Vehicle design issues. There are several potential means of actuating the aerodynamic maneuvering. The following approaches can be studied.

1. The use of pitch/roll/yaw thruster for lift vector angle control. This approach was applied in the simulations given in Section 5 because it did not require modifications to the existing aerodynamic data base.

2. Aerodynamic actuators (fins or wings). This involves a more significant re-design of the vehicle. Implementation of these approaches will require a modification of the control scheme as the vehicle will no longer be circularly symmetric. The simulation routines will require modification and the aerodynamic data base must be regenerated from first principles and/or similar vehicle data.
3. Proof mass actuation can be used to move the center of mass. This has the effect of changing the trim angle-of-attack, and therefore changes the lift coefficient. This is also a significantly different control approach as the controller now has control over the magnitude, as well as the direction, of the lift/side force vector.

Each of the above items affects more than the aeromaneuvering capabilities and controller design. The mission requirements, and the resulting packing configuration, will significantly influence which of these control options are available.

Control implementation. The simulation study used continuous-time measurements and a continuously variable thruster. It is more likely that a digital controller will be used and any thrusters may have a very coarse quantization, or even operate only in an on/off mode. This will affect the achievable control and will impact the resulting system performance.

Estimation Issues. The sensing required for adequate state estimation has not been addressed in this report. All controllers were designed under the assumption that they had access to the system state. The issue of errors in this estimation has yet to be considered and will have a potentially significant impact on the system performance. The estimation errors, as a function of time along the descent path, must be quantified for several sensing scenarios. Mease *et al.* [12] consider the state-estimation problem for a Mars aerocapture maneuver. This work serves as a good starting point in addressing the estimation problem for the precision landing scenario.

Robust estimation algorithms are required for the closed-loop estimation of the vehicle aerodynamic coefficients. These must be updated as a function of vehicle velocity and the errors associated with this update must be quantified.

During the initial part of the descent (down to about 60 km above the planet surface), the trajectory is essentially ballistic and there is almost zero control authority. It may be possible to use this period of time to update estimates of the atmospheric, gravitational and vehicle aerodynamic parameters.

Acknowledgements

This work was performed as a part of the Precision Landing task of the NASA funded Mars Exploration Technology Program at the Jet Propulsion Laboratory. The Mars Exploration Technology program is managed by Chuck Weisbin, and the Precision Landing task is managed by David Farless.

The control system development is managed by the Automation and Control section of JPL under Dr. Fred Hadaegh. The author also thanks Dr. Dhemitrios Boussalis of JPL for invaluable discussions and supporting work on this project.

References

- [1] T. A. Dierlam, "Entry vehicle performance analysis and atmospheric guidance algorithm for precision landing on Mars," 1990. MS thesis, Massachusetts Institute of Technology.
- [2] E. A. Euler, G. L. Adams, and F. W. Hopper, "Design and reconstruction of the Viking Lander descent trajectories," *J. Guidance & Control*, vol. 1, September-October 1978.
- [3] R. D. Braun and R. W. Powell, "Predictor-corrector guidance algorithm for use in high-energy aerobraking system studies," *AIAA J. Guidance, Control and Dynamics*, vol. 15, pp. 672-678, May-June 1992.
- [4] R. W. Powell and R. D. Braun, "Six-degree-of-freedom guidance and control analysis of Mars aerocapture," *AIAA J. Guidance, Control and Dynamics*, vol. 16, pp. 1038-1044, November-December 1993.
- [5] B. Etkin, *Dynamics of Atmospheric Flight*. Wiley & Sons, 1972.
- [6] D. Boussalis, "Equations of motion for aeromaneuvering re-entry vehicles," Tech. Rep. IOM 343-1171, Jet Propulsion Laboratory, February 1990.
- [7] D. Boussalis, "Longitudinal aerodynamic characteristics of a biconic re-entry vehicle," Tech. Rep. IOM 343-1173, Jet Propulsion Laboratory, March 1990.
- [8] D. Boussalis, "Lateral aerodynamic characteristics of a biconic re-entry vehicle," Tech. Rep. IOM 343-1177, Jet Propulsion Laboratory, March 1990.

- [9] R. D. Braun, R. W. Powell, W. C. Engelund, P. A. Gnoffo, K. J. Weilmuenster, and R. A. Mitcheltree, "Six degree-of-freedom atmospheric entry analysis for the Mars Pathfinder mission," in *AIAA 33rd Aerospace Sciences Meeting and Exhibit*, Jan. 1995. AIAA Paper # 95-0456.
- [10] D. A. Spencer and R. D. Braun, "Mars Pathfinder atmospheric entry trajectory design," in *AAS/AIAA Astrodynamics Specialist Conf.*, August 1995. AAS Paper # 95-379.
- [11] D. Enns, D. Bugajski, R. Hendrick, and G. Stein, "Dynamic inversion: An evolving methodology for flight control design," *Int. J. of Control*, January 1994.
- [12] K. D. Mease, A. K. Chatterjee, C. R. Purvis, and F. A. McCreary, "State estimation and parameter identification during aerocapture at Mars," in *AAS/AIAA Astrodynamics Specialist Conf.*, August 1987. AAS Paper # 87-505.